Contents lists available at ScienceDirect

Bioactive Materials

Imidazole functionalized photo-crosslinked aliphatic polycarbonate drug-eluting coatings on zinc alloys for osteogenesis, angiogenesis, and bacteriostasis in bone regeneration

Wei Zhang , Miao Dai , Ye Zhu [**] , Siyuan Li , Ying Sun , Xiaoya Liu , Xiaojie Li [*]

Key laboratory of synthetic and biological Colloids, Ministry of Education, School of Chemical and Material Engineering, Jiangnan University, Lihu Street 1800, Wuxi, 214122, China

A B S T R A C T

Zinc (Zn) alloys have demonstrated significant potential in healing critical-sized bone defects. However, the clinical application of Zn alloys implants is still hindered by challenges including excessive release of zinc ions (Zn^{2+}), particularly in the early stage of implantation, and absence of bio-functions related to complex bone repair processes. Herein, a biodegradable aliphatic polycarbonate drug-eluting coating was fabricated on zinc-lithium (Zn–Li) alloys to inhibit Zn^{2+} release and enhance the osteogenesis, angiogenesis, and bacteriostasis of Zn alloys. Specifically, the photo-curable aliphatic polycarbonates were co-assembled with simvastatin and deposited onto Zn alloys to produce a drug-loaded coating, which was crosslinked by subsequent UV light irradiation. During the 60 days long-term immersion test, the coating showed distinguished stable drug release and Zn^{2+} release inhibition properties. Benefiting from the regulated release of Zn^{2+} and simvastatin, the coating facilitated the adhesion, proliferation, and differentiation of MC3T3-E1 cells, as well as the migration and tube formation of EA.hy926 cells. Astonishingly, the coating also showed remarkable antibacterial properties against both *S. aureus* and *E. coli*. The *in vivo* rabbit critical-size femur bone defects model demonstrated that the drug-eluting coating could efficiently promote new bone formation and the expression of platelet endothelial cell adhesion molecule-1 (CD31) and osteocalcin (OCN). The enhancement of osteogenesis, angiogenesis, and bacteriostasis is achieved by precisely controlling of the released Zn^{2+} at an appropriate level, as well as the stable release profile of simvastatin. This tailored aliphatic polycarbonate drug-eluting coating provides significant potential for clinical applications of Zn alloys implants.

1. Introduction

For humans, skeletal system plays a pivotal role in providing structural support, maintaining mineral homeostasis, and protecting soft tissues and organs [1–3]. Despite the favorable regenerative capabilities inherent in bone tissue, reconstruction of critical-sized bone defects resulting from tumor, fractures, and congenital disorders remains a challenge [4–6]. Bone grafting is an effective treatment for bone defects, with autogenous bone grafting being widely regarded as the gold standard [7]. However, it has been gradually replaced by allogeneic bone grafting due to the discrepancies in donor size and shape, as well as the additional defects in the donor area [8,9]. Recently, due to the superior

machinability and biodegradability, significant interest has been paid on zinc (Zn) and its alloys as materials for bone grafting [3,10,11]. Additionally, Zn alloys exhibit a moderate degradation rate and produce neutral degradation products in simulated body fluid to prevent premature loss of mechanical properties required for implantation and reduce stimulation to surrounding tissue after implantation [12–15]. Among various available Zn alloys, zinc-lithium (Zn–Li) alloy is anticipated to provide sufficient mechanical integrity along with improved cytocompatibility, osteogenesis, and osseointegration during the healing process of bone fractures [16]. Therefore, Zn–Li alloy is regarded as one of the most promising materials for orthopedic transplantation [17, 18].

However, there remain two significant challenges for the clinical applications of Zn alloys implants. The first challenge is cytotoxicity arising from the burst release of Zn^{2+} in the early stage of implantation. The impact of Zn^{2+} on bone repair is dose-dependent: a low dosage stimulates osteoblast growth and differentiation, whereas a high dosage (~0.3 mM) exhibits cytotoxic properties towards osteoblasts [19–22]. Early implant failure can be caused by cytotoxicity and inflammation triggered by the rapid release of Zn^{2+} [23]. The second issue is the complex and multi-tiered bone repair processes, which involves hematoma formation, fibrocartilaginous callus formation, vascularization, and bony callus formation. The surface characteristics of Zn alloy are biologically inert and inadequate for these intricate bone restoration processes. Additionally, the bone defect healing and bone tissue regeneration processes are facilitated by synergistic interaction between osteogenesis and angiogenesis. Osteogenesis facilitates new bone formation, while vascular tissues can deliver necessary nutrients to bone tissues and promote the process of bone repair [24]. Both osteogenesis and angiogenesis contribute to the bone repair process. However, limited studies have been focused on developing osteogenic and angiogenic surfaces on Zn alloys [25]. Therefore, control the Zn^{2+} release dose and offer corresponding biological functions including antibacterial property to the surface of zinc alloy are crucial for the clinical application of zinc alloy.

In recent years, varieties of methods have been used in regulating the performance of Zn and its alloys for biodegradable implant applications. Zn/nano-SiC biocomposites prepared via pre-oxidation and selective laser melting exhibited enhanced mechanical properties and favorable biocompatibility on cell proliferation and adhesion [26]. Synergic controlling between strength and degradation of Zn alloys was well achieved through fine-grained manufacturing [27]. Besides, due to the intricately connection between tissues and surface characteristics of implants, surface modification still plays an important role in adjusting surface properties of Zn alloys while preserving their inherent bulk material performance. Recent advances in surface modification for orthopedic used Zn alloys included surface coatings [28–31], biomimetic deposition [32,33], stabilization treatment [34], microarc oxidation [35], atomic layer deposition [17], magnetron sputtering [36], and sandblasting [37]. Surface coating modification, especially polymer drug-eluting coatings, is an effective approach to regulate the degradation behavior of zinc alloys and accelerate the process of fibrocartilaginous callus formation and vascularization for medical implant. By releasing the drugs loaded in polymer coatings, a higher drug concentration at the implant location can be achieved, thereby facilitating the corresponding biological function post-implantation [38]. It has been reported that simvastatin (SIM) can increase osteoblast activity and enhance osteogenesis by upregulating the expression of recombinant bone morphogenetic protein 2 (BMP-2) in osteoblasts, while simultaneously downregulating tartaric acid phosphatase expression. Also, SIM has the ability to enhance the expression of vascular endothelial growth factor (VEGF), and promote vascular endothelial cell proliferation, differentiation, thereby stimulating angiogenesis [39]. Moreover, SIM exhibits broad-spectrum antibacterial properties [40]. Therefore, SIM is an ideal drug for drug-eluting coatings that introduce essential biological functions required for bone repair onto the surface of Zn alloy bone implants. Currently, most of the commercially available drug-eluting polymer coatings are based on natural macromolecules and bulk-eroding polymers, such as collagen [41] and poly(lactide-*co*-glycolide) [42]. The relatively rapid release of the encapsulated drug associated with multiphasic drug release profiles often limit their application in bone repair, where a slow and persistent drug release process is required. In contrast, aliphatic polycarbonates, especially poly(trimethylene carbonate) (PTMC), based drug-loaded coatings have a more predictable and controlled drug release profile due to their unique surface-eroding degradation behaviors, which can provide a sustainable drug release rate at the implant location [43]. Furthermore, the inherent hydrophobicity of PTMC and neutral degradation products minimize

their interference with loaded drugs [44]. Despite the advantages of PTMC, achieving a tailored aliphatic polycarbonates drug-eroding coating on Zn alloys with controlled release profiles for both loaded drugs and Zn^{2+} still remains challenging because of the limited affinity between commercially available PTMC and Zn^{2+}.

Recently, various types of metal-ligand (M-L) interactions have been employed for the efficient capture of bioactive metal ions [45,46]. Zn^{2+}-imidazole complexes is one of the widely present M-L complex in biological systems. It exhibits favorable bonding strength and enhanced moisture resistance, and can be used for applications in bone repair [47]. Therefore, the introduction of imidazole as pendant groups on PTMC to chelate Zn^{2+} is expected to partially inhibit excessive Zn^{2+} release by decreasing the diffusion rate of Zn^{2+} in the coating [48–50]. Moreover, the poor mechanical properties of PTMC could be overcome through the formation of cross-linked networks between Zn^{2+} and the imidazole pendant groups [51]. Therefore, by combining drug-loaded polycarbonate coatings with surface-eroding behavior, M-L interaction between imidazole groups and Zn^{2+}, and photo-crosslinking strategy, we envision the construction of mechanically robust drug-eluting coatings on Zn-alloy implants that exhibit consistent and stable corrosion resistance as well as controlled drug release properties. These coatings are intended to achieve multiple functions including long-term inhibition of Zn^{2+} release, promotion of osteogenesis and angiogenesis, and bacteriostatic effects.

In this study, a novel surface-eroding drug-eluting coating composed of SIM-loaded aliphatic polycarbonate photocurable coatings was prepared at the surface of Zn alloy. The coating shows enhanced integrity, sustained release of SIM and Zn^{2+}, as well as desirable bioactivities including osteogenesis promotion, angiogenesis induction, and bacteriostatic effects (Scheme 1). Aliphatic polycarbonate with imidazole and phenyl azido side groups (PTMCIA) was first synthesized, wherein imidazole and phenyl azido functioned as Zn^{2+} chelating agents and UV light curable moieties, respectively. Then, colloid particles (CPs) were prepared by self-assembly of PTMCIA and SIM. The drug loaded coatings were fabricated by electrophoretic deposition (EPD) of CPs on Zn alloys with subsequent photo-crosslinking. The chemical composition, surface morphology and adhesion strength of coatings were systematically characterized. The long-term immersion test was carried out to confirm the SIM releasing behavior and coating degradation mechanism. Finally, the biocompatible, osteogenic, angiogenic and antibacterial properties of the coatings were comprehensively investigated, and a rabbit critical-sized defects model was performed to evaluate the *in vivo* bone regenerative properties of the coating. The customized aliphatic polycarbonate drug-eluting coating enhanced the bone regeneration capability of Zn alloys by precisely controlling the release concentration of Zn^{2+} at an optimal level, while also ensuring a stable and controlled release of SIM with osteogenic, angiogenic, and antibacterial properties. This novel and versatile coating drug delivery system holds great potential for medical applications involving biodegradable metal implants.

2. Experimental section

2.1. Materials

Bis(pentafluorophenyl) carbonate (PFC, ≥98%), simvastatin (SIM, ≥97%) were obtained Aladdin Scientific, Ltd. (China). 2,2-Bis(hydroxymethyl)propionic acid (bis-MPA, ≥98%), cesium fluoride (CsF, 99%), benzyl alcohol (99.5%), *N*-boc-ethylenediamine (BocEA, ≥98%), triethylamine (TEA, ≥99.5%), *N*-(3-dimethylaminopropyl)-*N*′-ethyl-carbodiimide hydrochloride (EDC·HCl, 98.5%), triflic acid (98%), trifluoroacetic acid (TFA, 99%), and 1-(3-aminopropyl)imidazole (≥97%) were purchased from Macklin Scientific, Ltd. (China). 1,3-trimethylene carbonate (TMC, >98%) and 4-azidobenzoic acid (AzBA, ≥97%) were purchased from J&K Scientific, Ltd. (China). Poly(lactic-*co*-glycolic acid) (PLGA, $M_n = 60000$~80000 g mol^{-1}, LA:GA = 50:50) was obtained from Daigang Biomaterial Co., Ltd. (China). All other chemical
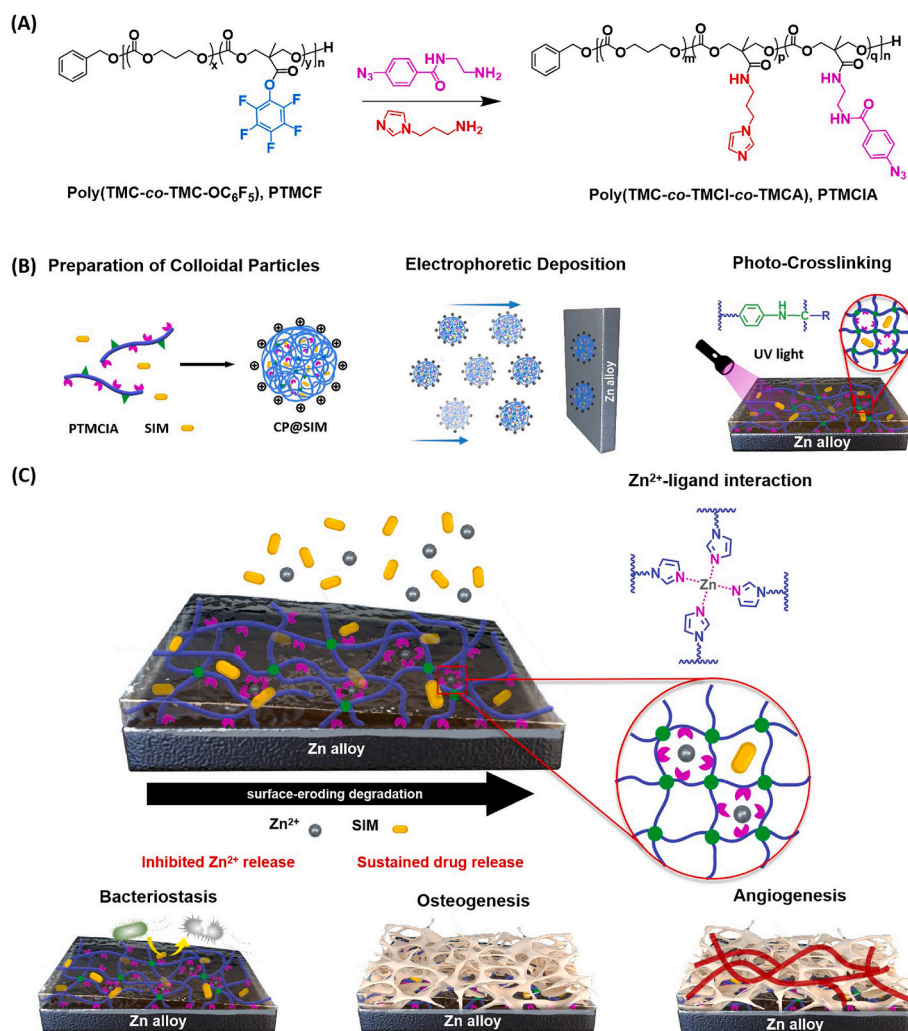
Scheme 1. Schematic illustration of the fabrication of photo-crosslinked aliphatic polycarbonate drug-eluting coating on Zn alloy. (A) Synthesis of the aliphatic polycarbonate poly(TMC-*co*-TMCI-*co*-TMCA) (PTMCIA). (B) Preparation of photo-crosslinked aliphatic polycarbonate drug-eluting coatings at the surface of Zn alloy. (C) The degradation and drug release process of polycarbonate coatings together with the osteogenesis, angiogenesis, and bacteriostasis of coated Zn alloy.

reagents were used as received. Zn–Li alloys were donated by the research group of Prof. Yufeng Zheng (Peking University, Beijing).

2.2. Synthesis of pentafluorophenyl ester functionalized six-membered cyclic carbonate (TMC-OC₆F₅)

According to the previous reported procedure (Scheme S1) [52], 100 mL round bottom flask was charged with 2,2-bis(hydroxymethyl)propionic acid (bis-MPA) (3.00 g, 22 mmol), bis-(pentafluorophenyl) carbonate (PFC) (21.70 g, 55 mmol, 2.5 eq.), CsF (0.7 g, 4.6 mmol, 0.2 eq.), and 70 mL anhydrous tetrahydrofuran (THF). After 20 h reaction at room temperature, solvent in the reaction mixture was removed, and the residue was dissolved in DCM, extracted and washed with sodium bicarbonate solution and deionized water respectively. The organic phase was then dried with $MgSO_4$ to obtain the crude product solution. After rotational evaporation, the product was recrystallized in ethyl acetate/hexane mixture solvent to obtain TMC-OC₆F₅ as a white crystalline powder. Yield: 4.75 g (64.8% yield). ^{1}H NMR (TMS, $CDCl_3$), δ ppm: 4.85 (2H, –O–CH_2–C–), 4.36 (2H, –O–CH_2–C–), 1.55 (3H, –CH_3).

2.3. Synthesis of the aliphatic polycarbonate copolymer poly(TMC-co-TMC-OC₆F₅) (PTMCF)

The synthesis process of PTMCF was carried out according to

literature procedures and the synthetic process is illustrated in Scheme S2 [52]. Take TMC-OC₆F₅/TMC feed ratio of 1:4 as an example. TMC-OC₆F₅ (2.608 g, 8 mmol, 20 eq.), TMC (3.264 g, 32 mmol, 80 eq.) and 8 mL anhydrous DCM were added into a 20 mL Schlenk flask, and the solution was homogenized by stirring. After three freeze-pump-thaw cycles, benzyl alcohol (0.8 mL, 0.5 M in DCM, 1 eq.) and triflic acid (70.76 μL, 0.8 mmol, 2 eq.) was added into the reaction tube under. After 24 h polymerization at room temperature, the reaction mixture was precipitated in diethyl ether twice and then dried under reduced pressure at 40 °C overnight. ^{1}H-NMR (400 MHz, $CDCl_3$), δ: 7.35–7.39 ppm (m, *Ph*CH_2O), 2.00–2.10 ppm (m, CH_2CH_2CH_2 of TMC unit), 4.18–4.27 ppm (td, OCH_2 of TMC unit), 4.44–4.48 ppm (s, OCH_2 of TMC-OC₆F₅ unit), 1.47–1.52 ppm (s, CH_3 of TMC-OC₆F₅ unit). GPC (RI): M_n (PDI) = 8.51 kDa (1.40).

2.4. Synthesis of azide modified molecule N-(2-aminoethyl)-4-azizanamide (AEAz)

The synthetic process is illustrated in Scheme S3. 4-azidazbenzoic acid (AzBA, 212.1 mg, 1.3 mmol) and *N*-tert-butylcarbonyl-ethylenediamine (BocEA, 256.0 mg, 1.6 mmol) were dissolved in 5 mL DCM. Then 1-(3-dimethylaminopropyl)-3-ethylcarbondiimine hydrochloride (EDC, 385 mg, 2.0 mmol) and triethylamine (TEA, 405.0 mg, 4.0 mmol) were added to the solution. After 12 h reaction at room temperature,

solvent in the reaction mixture was removed. The residue was dissolved in DCM, extracted with deionized water and dried by MgSO$_4$. After rotational evaporation, the product was recrystallized in diethyl ether, and light yellow powder was obtained. The light yellow powder was then dissolved in the mix solvent dichloromethane/trifluoroacetic acid (DCM: TFA = 1:1). After 0.5 h reaction, AEAz was obtained through rotational evaporation. ^{1}H NMR (TMS, CDCl$_3$), δ ppm: 7.84 (1H, *Ph*–C (O)–), 7.04 (1H, *Ph*–N$_3$), 3.53 and 3.41 (2H, –NH–C*H$_2$*–CH$_2$–), 1.42 (3H, –C*H$_3$*).

2.5. Synthesis of functionalized amphiphilic polycarbonate copolymer poly(TMC-co-TMI-co-TMCA) (PTMCIA)

First, poly(TMC-*co*-TMC-OC$_6$F$_5$) (1.7 g, 0.2 mmol) was dissolved in 10 mL anhydrous THF, and then 5 mL THF solution with dissolved AEAz (129.6 mg, 0.4 mmol, 0.1 eq. of TMC-OC$_6$F$_5$ unit) and TEA (834 μL, 1.5 eq. of TMC-OC$_6$F$_5$ unit) was added dropwise to the reaction solution in ice water bath. After that, the ice water bath was removed and the reaction mixture was reacted at room temperature for 1 h. Then, *N*-(3-aminopropyl) imidazole (828 μL, 5 M in THF, 1.15 eq. of residual TMC-OC$_6$F$_5$ unit) was added to the reaction mixture in ice water bath. After that, the ice water bath was removed and the reaction solution was reacted at room temperature for 2 h. The crude product was purified via directly repeated precipitation in diethyl ether, and dried under reduced pressure at 40 °C for 24 h ^{1}H-NMR (400 MHz, CDCl$_3$, δ: 7.84–8.00 ppm (m, TMC-CONHCH$_2$CH$_2$NHCO*Ph*N$_3$), 7.35–7.39 ppm (m, *Ph*CH$_2$O),7.57, 7.13, 6.87 ppm (3 s, TMC-CONHCH$_2$CH$_2$CH$_2$ imidazole), 4.18–4.26 ppm (s, OC*H$_2$* of TMC-CONHCH$_2$CH$_2$CH$_2$ imidazole and TMC-CON-HCH$_2$CH$_2$NHCOPhN$_3$), 4.10–4.18 ppm (td, OC*H$_2$* of TMC), 2.00–2.10 ppm (m, CH$_2$C*H$_2$*CH$_2$ of TMC), 1.04–1.15 ppm (s, C*H$_3$* of TMC-CONHCH$_2$CH$_2$CH$_2$ imidazole and TMC-CONHCH$_2$CH$_2$NHCOPhN$_3$). GPC (RI): M_n (PDI) = 12.62 kDa (1.56).

2.6. Preparation and characterization of colloidal particle solution

The acetone solution of PTMCIA at the concentration of 60 mg/mL was prepared. Then an appropriate amount of glacial acetic acid (the molar content was 50% of imidazole) was added over a period of 1 h to the polymer solution under magnetic stirring. After that, certain amount of SIM was added to the copolymer solution, and the final concentration of SIM was 1 mg/mL. Ultrapure water was added dropwise to the mix solution of PTMCIA and SIM to obtain SIM encapsulated colloidal particles (CP@SIM). Colloidal particles without SIM (CP) were prepared using the same method. The size and size distribution of CP@SIM and CP were determined by dynamic light scattering system (DLS), using a Brookhaven ZetaPALS particle size and zeta potential analyzer (Brookhaven Instruments Corp., USA). The morphologies of CP@SIM and CP were observed by scanning electron microscopy (SEM, Hitachi S-4800). To determine the SIM loading efficiency of CP@SIM, the colloidal particles solution was centrifuged under 8000 r min^{-1} for 1 h. After removing the supernation, the precipitate was dissolved in acetone and the SIM content was determined by ultraviolet–visible (UV–vis, TU-1901) spectroscopy at a wavelength of 238 nm. The SIM loading efficiency (LE) was calculated by the following equation:

$$LE = \frac{A_t - A_f}{A_t} \times 100\% \tag{1}$$

where the A_t is the total SIM amount, and A_f is the free SIM amount.

2.7. Preparation and characterization of CP@SIM coatings

Zn–Li alloy was polished with 1000# SiC sandpaper, and then ultrasonically cleaned three times in ethanol/acetone for 5 min. The CP@SIM dispersion served as the working solution to prepare EPD coatings. During the cathodic electrodeposition process, the substrate

was used as cathode and platinum as counter electrode with an electrode spacing of 20 mm. Wet films of CP@SIM were prepared on Zn alloy by deposition at 40 V for 4 min. After drying, the CP@SIM films were irradiated by a 254 nm UV light with a light intensity of 25 mW/cm^2 for 5 min. The SIM loaded PLGA coating and PTMC coating were prepared by dip-coating method. In particular, PLGA with hydroxyl groups on both ends was dissolved in DCM with concentrations of 1% (w/v). Certain amount of SIM was added to the PLGA solution, and the final concentration of SIM was 1 mg/mL. After dipping in the solution for 30 s, Zn alloy was withdrawn at a constant speed. This dip coating process was repeated three times with a 10 min time interval. Finally, the coated substrates were dried in the vertical position at 37 °C for 12 h to obtain the thickness-uniform films Zn-PLGA@SIM.

2.8. Characterization of CP@SIM coatings

The chemical composition of EPD coatings were investigated by attenuated total reflection Fourier-transform infrared spectroscopy (ATR-FTIR, Nicolet iS50) and X-ray photoelectron spectroscopy (XPS, Kratos Axis supra). The adhesion of coatings on Zn–Li alloy was determined by the lap-shear teat according to ISO-4587-2003 standard. Specifically, a pair of samples (60 × 10 × 2 mm^3) was stacked with an overlapped area of 20 × 10 mm^2 and glued with ergo 1309. The samples were then pulled in opposite directions at a speed of 1 mm/min until their detachment. The surface morphology of various samples was observed by SEM and wettability was determined by water contact angels (WCAs, Datephysics OCA15EC). The pencil hardness and adhesion strength of EPD coatings on Zn sheets were tested according to ISO 2409-2013 standard and ISO 14916 standard, respectively. The coating thickness at different deposition time was measured by an electronic thickness meter (Elcometer 456, Britain).

2.9. Electrochemical corrosion test and in vitro long-term immersion tests

The potentiodynamic polarization tests was conducted on an electrochemical workstation (CS350, Corrtest) with a typical three-electrode system. After soaking for 20 min in simulated body fluid (SBF), the corrosion current (I_{corr}) and corrosion potential (E_{corr}) values were measured with a scan rate of 1 mV/s and open-circuit potential from −0.6 to 0.6 V.

The *in vitro* immersion test was carried out at 37 ± 0.5 °C in SBF for 60 days to investigate the degradation and SIM release behavior of Zn-CP@SIM sample. Specifically, bare Zn alloy, Zn-PLGA@SIM and Zn-CP@SIM were immersed in 10 mL of SBF solution at pH 7.4. During the immersion tests, a 3 mL immersion solution from immersion system was substituted with 3 mL fresh SBF solution in real time. The SIM concentrations, pH values, and Zn^{2+} concentrations of immersion solution were determined via UV–vis spectroscopy, pH meter (OHAUS Starter 3100), and flame atomic absorption spectrophotometer (Varian AA240). After immersing for 0 and, 15, 30, 45, 60 days, the cross-section morphologies of Zn-CP@SIM samples were observed by SEM to determine the degradation rate. In particular, at 60 days immersion, the surface morphologies of bare Zn alloy, Zn-PLGA@SIM, and Zn-CP@SIM, were observed by SEM.

2.10. In vitro osteogenic activity

Osteoblast culture: Mouse calvaria-derived, pre-osteoblastic MC3T3-E1 (ATCC, CRL-2594) was used to investigate the cytocompatibility and osteogenic activity of samples. MC3T3-E1 was cultured in α-minimum essential medium (α-MEM, Gibco, US) supplemented with 10% fetal bovine serum (FBS, Gibco, US) and 1% penicillin-streptomycin (Biosharp, China) at a humanized atmosphere (37 °C, 5% CO$_2$). The culture medium was replaced every 3 days and 0.25% trypsin-ethylenediaminete-traacetic acid (Gibco, US) was used to cell dissociation while cells at high confluence (≥90%). After centrifuging at 1200

rpm for 5 min, cells were dispersed in fresh culture medium at an appropriate concentration for further study, which was divided into three groups: bare Zn alloy, Zn-CP and, Zn-CP@SIM.

Live/Dead staining assay: Cells with a density of 5×10^4/mL were seeded and cultured on the samples directly for 1 day and 3 days. At each time point, the cells were live/dead stained by FDA/PI, and cell spreading morphologies were observed with an upright fluorescence microscope (Nikon 80i, Japan).

Cell morphology: After 3 days of MC3T3-E1 culture, the cell structure was fixed in 4% (v/v) PFA for 30 min, permeated with 0.1% (v/v) Triton X-100 (Solarbio, China) for 5 min, then stained with 10 nM FITC-phalloidin solution (Solarbio, China) for 30 min. After cleaning with PBS three time, the cells re-stained with 10 μg/mL DAPI (4,6-diamino-2-phenylalanine, Solarbio, China) for 5 min. Finally, the staining results were observed using a fluorescence microscope. The live cell number and total coverage area were counted by Image J. SEM was used to further observed the cell morphology on different samples surface. The cells were fixed in 2.5% glutaraldehyde solution and dehydration in 70, 80, 90, and 100% ethanol solution.

Cell proliferation: An indirect cell proliferation test was conducted using the Cell Counting Kit-8 (CCK-8, MCE, US). Briefly, samples were soaking in the corresponding culture media at a ratio of 1.25 cm^2/mL for 3 days. The extract media was used to culture cells and CCK-8 solution was added into systems at 1 and 3 days. After incubating at 37 °C for 2 h, the cell proliferation was measured using a microplate reader (Biotek synergy H4, US) at a wavelength of 450 nm. Moreover, lactate dehydrogenase (LDH) cytotoxicity assay kit (Beyotime, China) was used to evaluate the cytotoxicity of different samples.

ALP activity and degree of mineralization: To determine the osteoinductive activity of different samples, MC3T3-E1 cells were cultured in an osteoinductive α-MEM medium, containing 50 μg/mL of ʟ-ascorbic acid (Sigma-Aldrich, Germany), 10 mM β-glycerophosphate (Macklin, China), and 100 nM of dexamethasone (MCE, US). After co-culture for 7 days, the cells were fixed 4% (v/v) PFA for 30 min, and then a BCIP/NBT alkaline phosphatase color development kit (Beyotime, China). The quantitative date was determined using ALP assay kit (Beyotime, China). Subsequently, on day 14, the degree of mineralization was examined using an Alizarin red S staining (ARS) osteogenesis assay kit (Beyotime, China). Cetylpyridinium chloride (10%) was used to dissolve the ARS and measured at 542 nm by a microplate reader.

2.11. Angiogenesis activity

In vitro cell migration and tube formation assays: An indirect assay was carried out to determine the angiogenesis activity of different samples. The supernatants of differentiated MC3T3-E1 culture system from the blank, and bare Zn, Zn-CP, Zn-CP@SIM groups were collected to culture the human endothelial cell line EA.hy926 (ATCC, CRL-2922) until reaching about 90% confluence. And then 100 μL pipet tip was used to create a crack in the middle of the well. The exfoliated cells were rinsed by PBS three times and the fresh media with free FBS was added. The cells were photographed at 24 h. Moreover, cell tube formation assay was carried out according to a classical method. Briefly, 5×10^4 stimulated EA.hy926 were seeded in a 96-well plate, which have pre-laid 50 μL of growth factor-depleted Matrigel (ABW, China) and cured. After incubation for 6 h, the tube formation was observed by an inverted microscope (ZEISS Axio Vert A1, Japan). The quantitative analysis was counted by Image J.

In vivo angiogenesis of CAM: A modified chicken chorioallantoic membrane (CAM) assay was used to evaluate the angiogenesis *in vivo*. Specifically, the fertilized eggs were incubated in humanized atmosphere (temperature 37.8 °C, humidity 80%). After incubating for 4 days, a hole was created at the top end of egg, and 3-4 mL albumen was sucked out. Then the hole was sealed by an adhesive tape. When incubating for 9 days, bare Zn alloy, CP coated Zn alloy, and CP@SIM coated Zn alloy were implanted. All the procedures were carried out under

aseptic conditions. On day 12, images were taken and analyzed by Image J software.

2.12. In vitro antibacterial experiments

The spread plate method *S. aureus* (Gram-positive, ATCC-6538)) and *E. coli* (Gram-negative, ATCC-700926)) as bacterium models was conducted to evaluated the antibacterial activity of the samples. 316L stainless steel (316L SS) was served as control group. Specifically, 2 mL of the bacterial solution containing 1×10^6 CFU/mL and samples were co-incubated in 10 mL 0.9% NaCl solution at 37 °C for 12 h. Then the samples were rinsed by fresh 0.9% NaCl solution three times to remove non-adherent bacteria and sonicated in 10 mL 0.9% NaCl solution for 10 min to obtain bacterial suspension. After diluting 1000 times, 100 μL of the bacterial suspension were uniformly plated onto LB agar plates and cultured for 12 h at 37 °C. Finally, the number of colonies on the LB agar plates was counted. And the antibacterial rate was calculated as follows:

$$\text{Antibacterial rate } (\%) = \frac{\text{CFU}_C - \text{CFU}}{\text{CFU}_C} \times 100\% \tag{2}$$

where CFU$_C$ and CFU denote the number of colonies of and that of either bare or coated Zn alloy, respectively.

The SEM was used to examined the morphologies of bare Zn alloy-treated and CP@SIM coated Zn alloy-treated bacteria. Briefly, bacteria were incubated with samples for 2 h, and then fixed with 2.5% glutaraldehyde for 10 min. Subsequently, the samples were dehydrated with a graded ethanol series.

2.13. In vivo experiments

All procedures of the experiment were approved and in accordance with the committee of the Wuxi Experimental Animal Association. Rabbit critical-size femur bone defects model was performed to verify the biocompatibility, osteogenesis, and angiogenesis of the samples. New Zealand white rabbits (2.5–3 kg) were acclimatized for 1 week and divided into three groups (bare Zn alloy group, Zn-CP group, and Zn-CP@SIM group, each group had 4 rabbits). After anaesthetizing by ear vein injection of 2% pentobarbital sodium, a 9 mm depth, 5 mm diameter of defect was created on the thigh femur with hand drill. The implant (size: 5 mm × 9 mm) was placed and the wound was carefully sutured. After 8 weeks, the rabbits were sacrificed. The thigh femur was removed together with the implant and fixed with 4% (v/v) PFA solution for subsequent Micro-CT, hematoxylin and eosin (H&E), Masson's trichrome, and immunohistochemical staining (CD31 and OCN).

3. Results and discussion

3.1. Preparation and characterization of imidazole functionalized photo-crosslinked CP@SIM coatings

The photo-curable aliphatic polycarbonate (PTMCIA) with dual functionality of imidazole and phenyl azido was synthesized via organocatalytic ring-opening polymerization (OROP) of 1,3-trimethylene carbonate (TMC) and a cyclic carbonate monomer containing an active pentafluorophenyl ester group (TMC-OC$_6$H$_5$), followed by post-polymerization functionalization. The resulting PTMCIA comprised a 14 mol% imidazole functionalized moiety and a 6 mol% phenyl azido functionalized moiety (Scheme 1A). The synthesis details and characterization results are shown in Scheme S1-S3 and Figs. S1–S5. Through the hydrophobic interactions, SIM loaded PTMCIA colloidal particles (CP@SIM) were prepared by self-assembly of PTMCIA together with SIM (Fig. S6). The CP@SIM were spherical with approximately 180 nm diameter and positive charged surface (Fig. S7). The PTMCIA colloidal particles (CP) without SIM were prepared as a control.

The CP@SIM coatings at the surface of Zn alloy was prepared by the

electrophoretic deposition (EPD) method [51], as shown in Fig. 1A. The thickness of the coatings can be controlled by regulating deposition time and colloidal concentration (Fig. 1B). As shown in Fig. S8, digital photos of CP@SIM coated Zn alloys exhibited good uniformity, and the colors of coatings before and after UV light irradiation was observed, indicating the photo-crosslinking of phenyl azido groups and formation of amide bonds [53]. Furthermore, attenuated total reflection Fourier-transform infrared spectroscopy (ATR-FTIR) was used to monitor the curing process of CP@SIM coating under the UV light irradiation (Fig. S9). The characteristic peak of phenyl azido groups at 2130 cm^{-1} completely disappear after a 5 min UV light irradiation (Fig. 1C), indicating a

complete photo-crosslinking of the coatings. The schematic illustration of a possible mechanism for the photochemical reaction of phenyl azido groups was shown in Scheme S4 [54]. The basic coating properties of Zn-PTMC$_{100000}$, Zn-CP and Zn-CP@SIM was shown in Table S1. 1. The surfaces of the crosslinked Zn-CP and Zn-CP@SIM samples exhibited increased hardness compared to the uncross-linked Zn-PTMC sample, and SIM had no impact on the hardness of the coating.

The insufficient bonding between the metal and polymer coating is an inherent constraint that may lead to coating delamination. The optimization of adhesion strength between aliphatic polycarbonate coatings and Zn alloys was of paramount importance. The adhesion
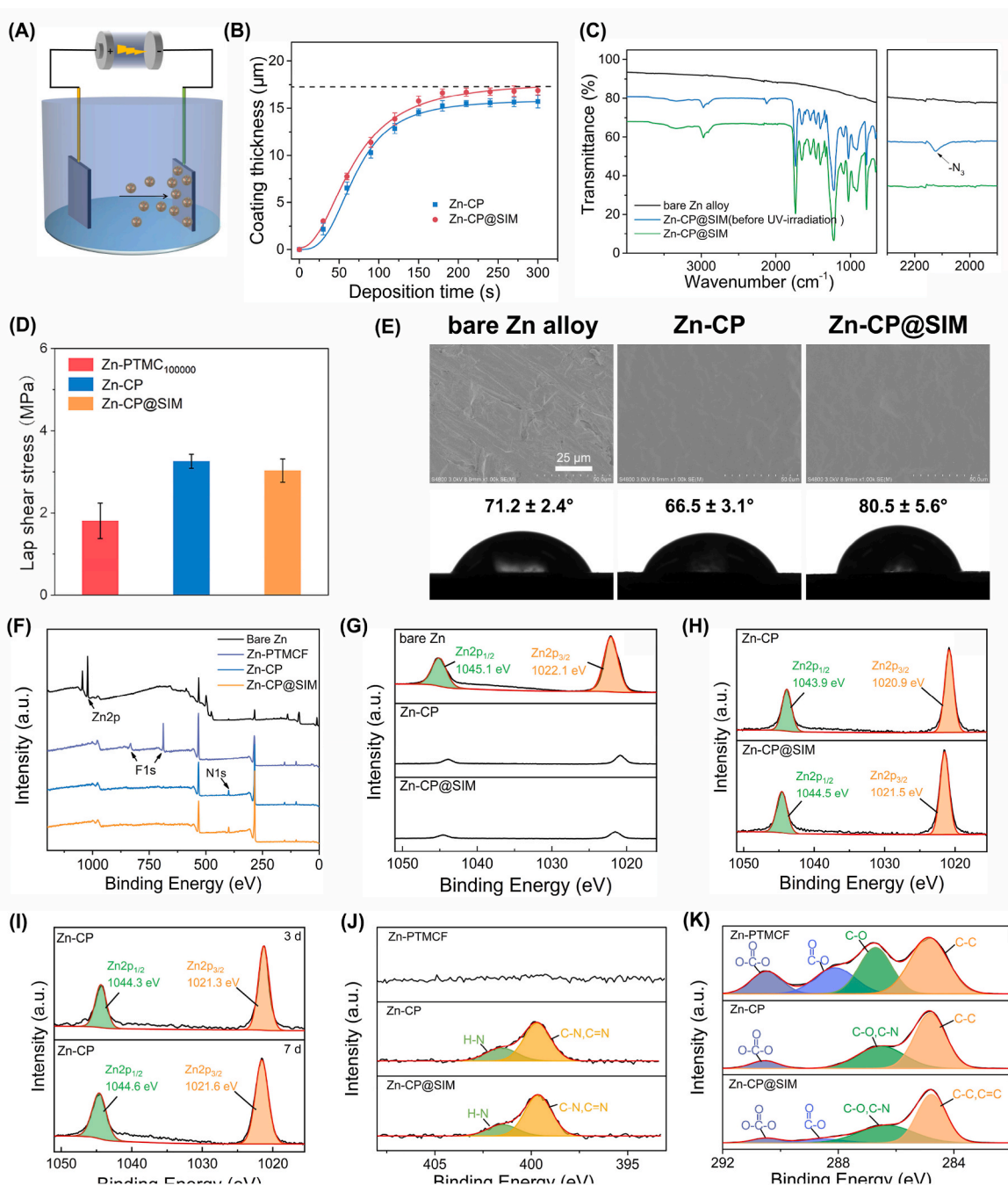

Fig. 1. (A) Schematic illustration of electrophoretic deposition of CP@SIM colloidal particles on a Zn alloys substrate. (B) Coating thickness for varying time at a constant voltage of 40 V and a colloidal concentration of 15 mg/mL (C) ATR-FTIR spectra of bare and CP@SIM coated Zn alloys before and after UV light irradiation. (D) Lap shear stress of PTMC, CP, and CP@SIM coating on Zn alloys. (E) SEM and WCAs images of bare, CP, and CP@SIM coated Zn alloys. (F) XPS wide-scan, (G) and (H) Zn 2p spectra of bare and CP, CP@SIM coating on Zn alloys, (I) Zn 2p spectra of CP coating on Zn alloys after 3 and 7 days immersion, and (J) N 1s, (K) C 1s spectra of PTMCF, CP, and CP@SIM coated Zn alloys.

strength of CP@SIM coating was 3.01 MPa, which increased 59.3% compared to the commercially-available PTMC coating (Fig. 1D). This was mainly attributed to the application of EPD method together with photo-crosslinking [51]. On one hand, the high throwing power of EPD technology enables colloidal particles to effectively fill small pores and gaps on the substrate surface, creating numerous physical anchoring points between the coating and the substrate [55]. The crosslinking process, on the other hand, enhances the cohesion of the coating and prevents potential damage to its internal structure during testing. The surface morphology, hydrophilicity and surface chemical composition of the coatings were further characterized. As shown in Fig. 1E, numerous scratches caused by polishing were observed at the surface of bare Zn alloy. In contrast, the surfaces of Zn-CP and Zn-CP@SIM were uniform and smooth, indicating that coatings on Zn alloys were successfully prepared through EPD method. Compared with Zn-CP, the contact angle of drug loaded Zn-CP@SIM significantly increased from $66.5° \pm 3.1°$ to $80.5° \pm 5.6°$, due to the present of hydrophobic drug SIM. Surface elemental analysis by XPS was shown in Fig. 1F. The Zn 2p peaks at 1045 eV and 1022 eV was observed in bare Zn alloy and CP and CP@SIM coated Zn alloys (Fig. 1G). Due to the uniform coverage of coatings on the substrate surface, the peak intensity of CP and CP@SIM coated Zn alloys was significantly reduced. After 3 and 7 day immersion, no

observable change was detected for the Zn 2p spectra of Zn-CP (Fig. 1I). Compared with aliphatic polycarbonate copolymer poly(TMC-*co*-TMC-OC$_6$F$_5$) (PTMCF) coated Zn alloys, a new peak of N 1s at 399.1 eV was detected on CP and CP@SIM coated Zn alloys, while the peaks of F 1s at 687.8 and 833.1 eV was disappeared. Specifically, the peaks at 399.7 eV (C–N, C=N) and 401.6 eV (N–H), corresponding to the imidazole groups and amido moieties after post-polymerization functionalization, were observed in N 1s spectra of CP and CP@SIM coatings (Fig. 1J). Significantly, in the C 1s spectra of CP@SIM coatings, the peak corresponding to ester bond (C(O)–O) of SIM molecules at 288.6 eV was detected (Fig. 1K), indicating the successful loading of drugs. Via calculating integral area of ester bond, surface SIM content was 2.7 wt%.

3.2. Electrochemical corrosion test and in vitro long-term immersion tests

The polarization curves of bare Zn alloy, Zn-CP, and Zn-CP@SIM in simulated body fluid (SBF) were tested, and the corrosion potential (E_{corr}) and corrosion current (I_{corr}) of each sample in the polarization curves were fitted using the Tafel method (Fig. 2A). The corrosion potential of bare Zn alloy, Zn-CP, and Zn-CP@SIM samples increased while the corrosion current of those decrease, suggesting an enhancement in corrosion resistance for all coatings. The Zn-CP@SIM sample exhibited
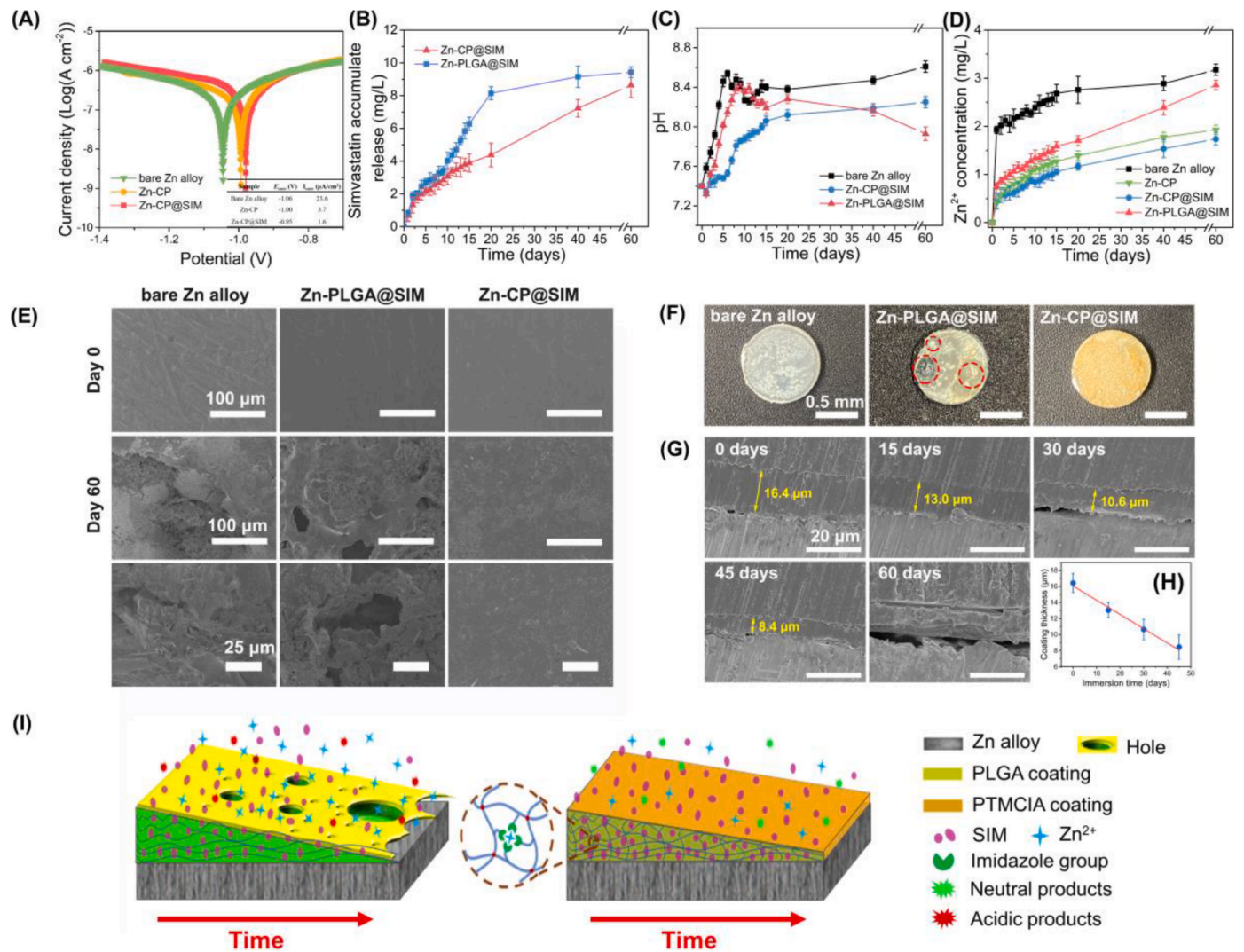
Fig. 2. (A) Potentiodynamic polarization test of bare and coated Zn alloys in SBF (37 ± 0.5 °C) for 4 h. (B) SIM accumulates release curves for coated Zn alloys. (C) pH values, (D) Zn^{2+} concentrations, (E) surface SEM images, (F) digital photographs, and (G) cross-sectional SEM images of bare and coated Zn alloys after immersion for 60 days in SBF at 37 °C. (H) Fitted curve of CP@SIM coating thickness after immersing for 0 and, 15, 30, 45 days. (I) Schematic illustration of degradation and drug release process of coated Zn alloys.

the best corrosion resistance, it is because the introduction of hydrophobic drug SIM enhanced the hydrophobicity of coatings, and further reinforced the physical barrier effect of the coating against corrosive media.

A static immersion test was conducted to determine the drug release and degradation behavior of CP@SIM coatings. Considering that PLGA coating has been widely used in orthopedic drug-eluting implant [56], a SIM -loaded PLGA coating (PLGA@SIM) was prepared on the surface of Zn alloys as a comparison. The SIM content in the extracts of coated samples was monitored by UV–vis spectroscopy. The maximum UV absorption of SIM was 238 nm and the standard curve determined at this wavelength showed good linearity (Fig. S11). As shown in Fig. 2B, CP@SIM coated sample showed a two-phase release profile with a burst release of SIM during the first 3 days, followed by a sustained and slower drug release in the later 57 days immersion. In comparison, PLGA@SIM coated Zn alloys exhibited a comparable drug release profile to CP@SIM coated Zn alloys in first 3 days. However, an abrupt accelerated drug release occurred from 10 to 20 days, and then drug release significantly decreased last from 25 to 60 days. Furthermore, the pH values and Zn^{2+} concentrations of immersion solutions were measured by pH meter and flame atomic absorption spectrophotometer, respectively. According to previous study [57], the corrosion process of Zn–Li alloy immersed in SBF solution was shown in S1–S7. Initially, during the early stage of immersion, the Zn alloy underwent a reaction with oxygen, leading to the substantial release of Zn^{2+} and OH^-. This process resulted in a swift elevation of the Zn^{2+} concentration and pH value within the immersion system, which was also the main reason for the high cytotoxicity of the Zn alloy. Subsequently, as the pH in the system increased to a specific value, Zn^{2+} and OH^- reacted to form the insoluble corrosion products Zn $(OH)_2$ and ZnO. The consumption of OH^- caused a certain decrease in the pH of the system. However, the presence of Cl^- in the immersion system hindered the reaction, causing the conversion of corrosion products on the surface of the Zn alloy into soluble $ZnCl_2$. In addition, Zn^{2+} would also react with $H_2PO_4^{2-}$ and HCO_3^- in the solution, resulting in the formation of insoluble phosphates and carbonates. As shown in Fig. 2C, both bare and PLGA@SIM coated Zn alloys showed a rapid pH value increase in the first 10 days due to the rapid degradation of Zn alloy substrate [58], while relatively lower pH values were observed for CP@SIM coated Zn alloys. It should be noted that, different form the bare and CP@SIM coated Zn alloys, PLGA@SIM coated Zn alloys exhibited a gradual downward pH trend in the subsequent 50 days immersion, which was most probably due to the continuous release of acidic degradation products from the PLGA coating. Regarding the Zn^{2+} release (Fig. 2D), as expected, coated Zn alloys exhibited a much lower Zn^{2+} release rate than bare Zn alloy, and the Zn^{2+} release rate of CP@SIM coated Zn alloys was much lower than PLGA@SIM coated Zn alloys. The effective barrier provided by the coating against corrosive media is attributed to the inhibition of Zn alloy degradation. In comparison to bulk-eroding PLGA@SIM coating, surface-eroding CP@SIM coating demonstrateed superior corrosion protection for Zn alloys by effectively blocking corrosive media. Additionally, the chelation between Zn^{2+} and imidazole in the CP@SIM coating effectively hindered the release of Zn^{2+} to a certain extent. The surface and cross-section morphologies of bare and coated Zn alloys samples before and after immersion were observed by SEM and presented in Fig. 2E. The surface of bare Zn alloys was fully covered with corrosion products after 60 days immersion. The PLGA@SIM coating exhibited numerous hole defects as a result of the bulk degradation of PLGA and the formation of its acidic byproducts [59]. The CP@SIM coated Zn alloys, in contrast, maintained a smooth and uniform surface due to the exceptional adhesion, efficient photo-crosslinking, predictable degradation behavior of CP@SIM coatings, and the robust chelation interactions between imidazole groups and released Zn^{2+}. A similar phenomenon was also observed in the digital photographs of samples after immersion for 60 days. (Fig. 2F). The cross-section morphologies of CP@SIM coated Zn alloys after immersion for 0, 15, 30, 45 and 60 days were shown in Fig. 2G. At 0–45

days, the coatings had distinct boundaries and good integrity. However, as the coating gradually degraded, the integrity and protective capabilities of the coating were progressively compromised. Especially at day 60, the boundaries of the coating became extremely difficult to determine due to the presence of large amounts of corrosion products and hollows. As shown in Fig. 2H, the coating thickness decreased from 16.4 to 8.4 μm with an average degradation rate of 0.18 μm per day, demonstrating the surface-erosion degradation mechanism of CP@SIM coatings. These results agreed with the envision that imidazole functionalized photo-crosslinked aliphatic polycarbonate drug-eluting coatings could more efficiently regulate the long-term drug release compared with PLGA drug-loaded coating. Fig. 2I presented a schematic illustration of degradation and drug release mechanism of PLGA@SIM and CP@SIM coatings. Firstly, cracks and micropores were formed in PLGA coating owing to its self-accelerated bulk degradation, and then the protective effect of PLGA coating would be destroyed, resulting in failing to control the drug and Zn^{2+} release. And the released acidic degradation products like lactic acid would accelerate this process. Therefore, an accelerated SIM release profile was observed for PLGA@SIM coatings from 8 to 20 days. Conversely, the distinctive surface-erosion properties with neutral degradation products allowed the CP@SIM coating to maintain a long-term barrier effect to the corrosive media, resulting in a well-controlled drug release and outstanding anti-corrosion performance to the Zn alloy substrate. Moreover, the imidazole groups in CP@SIM coating could further regulate Zn^{2+} release by the strong chelation effects.

3.3. In vitro cell viability and cell morphology

The cytocompatibility of Zn alloy implants plays a crucial role in the process of bone regeneration. Herein, the mouse preosteoblastic cells MC3T3-E1 were directly cultured at the surface of bare and coated Zn alloys to assess their cell adhesion and proliferation performance. The fluorescence micrographs of live/dead staining of MC3T3-E1 cells using PI and FDA dyes after 1 and 3 days incubation were shown in Fig. 3A. The green and red fluorescence represented the nuclei of living and dead cells, respectively. Dead cells on the surface of bare Zn alloys were observed after1 day culturing, and the number of dead cells increased after 3 days culturing. In contrast, no dead cells was observed on surface of the CP and CP@SIM coated Zn alloys. The cell proliferation and cytotoxicity of CP and CP@SIM coated Zn alloys were quantitatively determined using the Cell Counting Kit-8 (CCK-8) and lactate dehydrogenase (LDH) activity assay, as shown in Fig. 3B and C. As shown in Fig. 3B, the absorbance at 450 nm of bare Zn alloys group increased from day 1 to day 3. In contrast, both coated Zn alloys groups exhibited a significant enhancement, which was consistent with the findings of the live/dead assay. Furthermore, the LDH activity of both coated Zn alloys groups displayed a lower cytotoxicity compared to bare Zn alloys group. The above results demonstrated that the application of aliphatic polycarbonate coating effectively reduced the cytotoxicity of Zn alloys, primarily due to the excellent cytocompatibility of aliphatic polycarbonate coatings and the suppression of Zn^{2+} release.

It has been reported that an appropriate amount of Zn^{2+} could promote the colonization and spread of osteoblasts [20]. However, excessive Zn^{2+} released from bare Zn alloys may inhibit the cell spreading, and further delay the bone regeneration process [13]. Therefore, FITC-phalloidin/DAPI fluorescence staining combined with SEM were applied to observe the morphology of MC3T3-E1 cells after cultured on bare and coated Zn alloy samples for 3 days. As shown in Fig. 3D and E, as expected, due to the excessive Zn^{2+} release, MC3T3-E1 cells cultured on bare Zn alloy exhibited a round and shrunken shape. However, the cells cultured on coated Zn alloys showed a plump and polygonal morphology with many cell processes and pseudopodia, suggesting a further differentiated morphology. Fig. 3F and G were the quantitative analysis results of phalloidin/DAPI fluorescence photographs. The CP@SIM coated Zn alloys showed the highest live cell numbers and
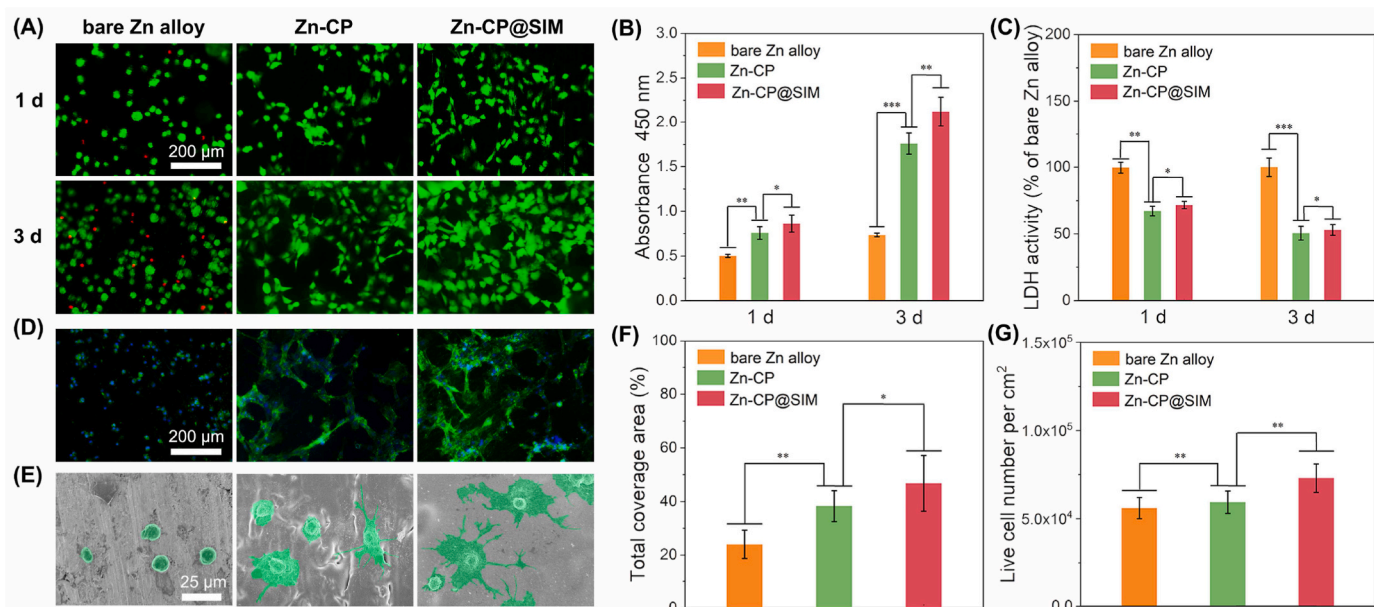
Fig. 3. Viability and morphology of preosteoblast MC3T3-E1 on bare, CP coated, and CP@SIM coated Zn alloys. (A) Live/dead stained fluorescence images for MC3T3-E1 on different samples after culturing for 1 and 3 days. (B) Cell viability by CCK-8 and (C) LDH activity of MC3T3-E1 incubated in different extracts for 1 and 3 days. (D) Fluorescence images of MC3T3-E1 cultured on different sample surfaces for 3 days with action stained with FITC (green) and nuclei stained with DAPI (blue). (E) SEM images of MC3T3-E1 cultured on different sample surfaces for 3 days. (F) Total coverage area and (G) number of live cells. $*p < 0.05$, $**p < 0.01$, $***p < 0.001$.

largest coverage. It has been reported that biochemical signals between osteoblasts and osteocytes could be transferred by their intercellular connectivity, which would affect the formation of functional syncytial network by interconnected osteocytes in mature bone [60]. Besides, compared to CP coatings, CP@SIM coatings not only maintained a lower level of Zn^{2+} release, but also achieved a stable release of SIM, both of which combined might enhance cell adhesion, growth, and proliferation to a certain extent. Therefore, CP@SIM coating could definitely improve the cytocompatibility of Zn alloys, promote the proliferation and

adhesion of osteoblasts, and be well-suited for bone regeneration.

3.4. In vitro osteogenic ability

After culturing on bare and coated Zn alloys for 7 and 14 days respectively, the osteogenic potential of Zn alloy samples was evaluated by measuring the differentiation and mineralization degree of MC3T3-E1 cells using alkaline phosphatase (ALP) activity assay and alizarin red staining (ARS). The representative staining photographs of bare, CP
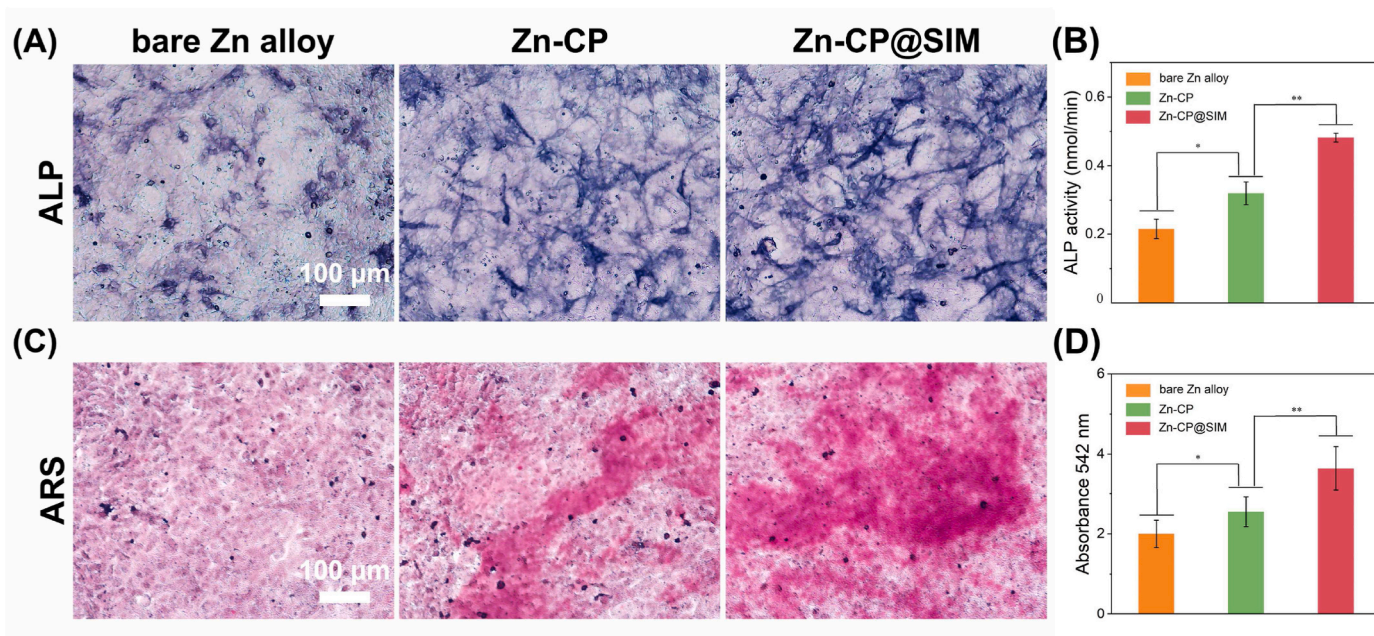

Fig. 4. Osteogenic activity *in vitro* of the different Zn alloys. (A) Representative staining photographs and (B) quantification of ALP activity for MC3T3-E1 cultured on different samples for 7 days. (C) Representative ARS staining photograph and (D) quantification of calcium deposition for MC3T3-E1 cultured on different samples for 14 days. $*p < 0.05$, $**p < 0.01$, $***p < 0.001$.

coated, and CP@SIM coated Zn alloys were shown in Fig. 4A and B. After culturing for 7 days, both the coated Zn alloys, particularly the CP@SIM coated ones, exhibited a more intense ALP staining compared to the bare Zn alloys. Furthermore, ARS staining demonstrated the formation of mineral nodules, where the coated Zn alloys exhibited much denser calcified nodules after culturing for 14 days, indicating the extracellular matrix mineralization on coated Zn alloys was significantly greater than that on bare Zn alloys. The above results were confirmed by quantitative analyses that both CP and CP@SIM coated samples had a higher ALP activity and mineralization degree than bare samples, while CP@SIM coated Zn alloys showed the best *in vitro* osteogenic performance (Fig. 4C and D). This was probably because the controlled release of osteogenic drug SIM combined with relatively low dose of Zn^{2+} could enhance differentiation of osteoblasts [61].

3.5. Angiogenic ability

During the bone defect healing and bone tissue regeneration, angiogenesis and osteogenesis were tightly interrelated. And moderate zinc ion and SIM have been reported that could promote angiogenesis in bone regeneration [39,62]. Therefore, other than the osteogenic activity, angiogenic activity of CP@SIM coated Zn alloys were investigated by migration assay, tube formation assay and *in vivo* chicken embryo allantoic membrane (CAM) assay. After a scratch wound was created by a 100 µL pipette tip, endothelial cells EA.hy926 were cultured in serum-free medium for 12 h. In Fig. 5A, the photographs of EA.hy926 after culturing for 0 h and 12 h were presented. Comparing with culturing for 0 h, it was apparent that the gaps were significantly shrinking at 12 h due to the migration of EA.hy926, especially for Zn-CP and Zn-CP@SIM group. And the number of endothelial cells migrated into the scratches to close the gap was counted (Fig. 5B). Obviously,

more than 160 endothelial cells were counted in Zn-CP@SIM group, which far more than the number of bare Zn and Zn-CP group. Tube formation assay as a classic method was used to evaluate the effect of CP@SIM coated Zn alloys in the angiogenesis of endothelial cells *in vitro*. As shown in Fig. 5C, it could be observed that the capillary-like networks with favorable morphological characteristics of Zn-CP@SIM group was richer than that of any other groups. The statistical analysis for the number of tubes was presented in Fig. 5D, which was consistent with the observations. These results indicated that the Zn-CP@SIM sample could promote the spontaneous migration and aggregation of EA.hy926 to form a capillary network with a certain structure, which was conducive to angiogenesis during bone regeneration. Based on *in vitro* angiogenic assay, imidazole functionalized aliphatic polycarbonate coated Zn alloys were prima facie confirmed to promote angiogenesis, which was greatly enhanced by the introduction of SIM. Subsequently, *in vivo* CAM assay was used to further confirm the angiogenesis of Zn-CP@SIM (Fig. 5E and F). After co-culturing for 5 days, only limited angiogenesis was observed in the bare Zn alloy group. This was because the excess Zn^{2+} released by the bare Zn alloy caused obvious toxicity to the surrounding vascular tissue, leading to gradual ablation of the vascular tissue. In contrast, the vascular networks of the coated samples were clearly visible. Blood vessels could provide nutrients for the survival, growth, and development of chicken embryos. It was noteworthy that CP@SIM coated Zn alloy group showed the richest vascular networks and most intersections of the neovessel, representing better angiogenesis. Overall, based on the dually controlled release effect of Zn^{2+} and SIM release control, CP@SIM coated Zn alloys could infinity eliminate the toxicity of Zn alloys and promote the angiogenesis in bone repair process, which would be a promising choice for regeneration of neuro-vascularized bone tissue.
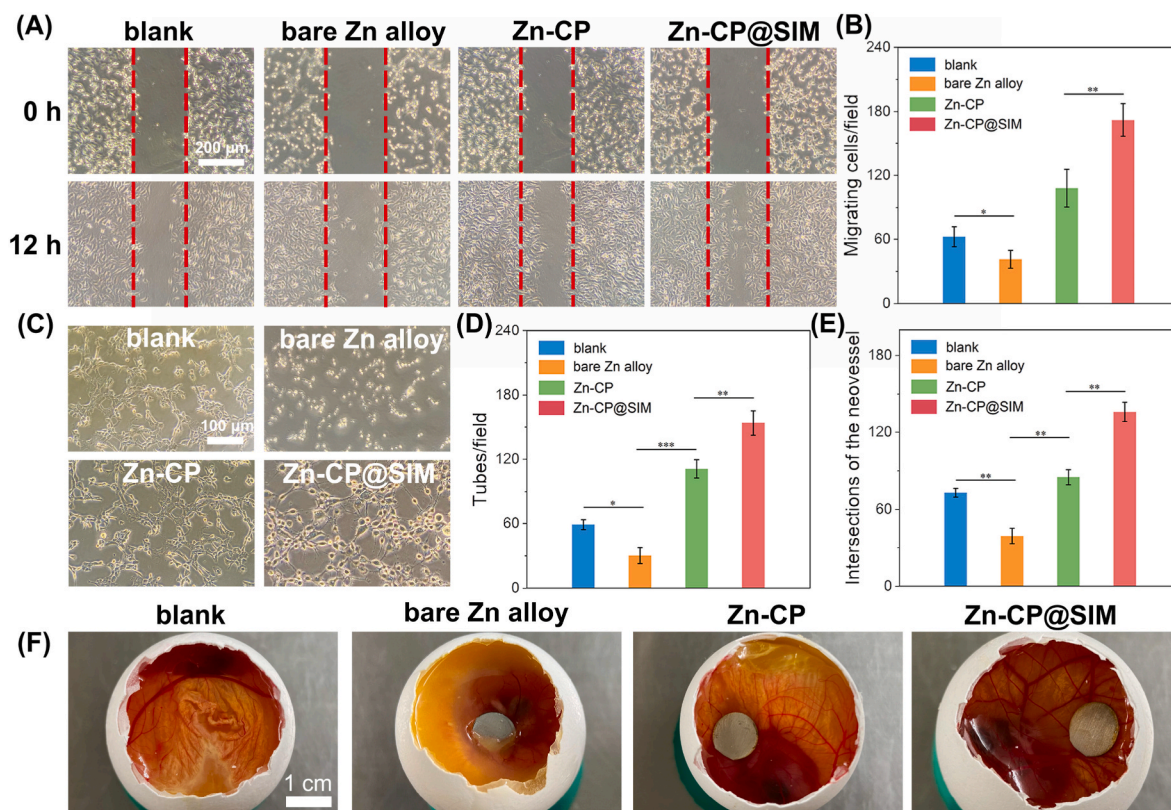

Fig. 5. Angiogenic activity of the different Zn alloys samples. (A) Migration assay of EA.hy926 incubated with the extract of different samples after wounding. (B) Quantification statistical analysis of migration assay. (C) Tube formation assay of EA.hy926 in different extracts cultured on Matrigel. (D) Quantification statistical analysis of tube formation assay. (E) Quantification statistical analysis of *in vivo* CAM assay. (F) Representative photographs of *in vivo* CAM assay. *$p < 0.05$, **$p < 0.01$, ***$p < 0.001$.

3.6. In vitro antibacterial ability

The recent studies have testified that SIM possess good antibacterial ability by destroying the functional membrane microdomains of bacteria to inhibit the bacterial growth and biofilm formation [40]. This may achieve the enhanced antibacterial effect with Zn^{2+}. Specifically, high doses of Zn^{2+} had strong antibacterial activity but exhibited significant cytotoxicity [63]. To balance antibacterial activity and cytocompatibility, SIM with broad-spectrum antibacterial properties was introduced to compensate for the insufficient antibacterial ability of low-dose Zn^{2+}. Therefore, the mechanism of the enhanced antibacterial effect was that SIM as a potent antibacterial agent combined with low-dose Zn^{2+} with low antibacterial activity jointly exhibited better antibacterial ability. To demonstrate the above antibacterial mechanism, the antibacterial ability of Zn-CP@SIM were evaluated with 316L SS served as positive

control group. As shown in Fig. 6A–C, due to the antibacterial activity of Zn^{2+}, the bare Zn alloy exhibited the antibacterial rates of 75.8% and 88.5% against *E. coli* and *S. aureus*, respectively. As expect, antibacterial capacity of Zn-CP was inferior to bare Zn alloy, which was attributed to the suppressed Zn^{2+} release and low toxicity of coating. In contrast, with the introduction of SIM, the antibacterial properties of Zn-CP@SIM were greatly enhanced with antibacterial rates exceeding 95% against to both *E. coli* and *S. aureus*. This could be attributed to the combined antibacterial effect of released Zn^{2+} and SIM. The antibacterial process of the Zn-CP@SIM samples were further studied by observing the cell membrane integrity and morphology of bacteria (Fig. 6D). The bacteria adhered to the bare Zn alloy presented normal cellular morphology with a smooth surface. In contrast, only a few numbers of bacteria adhered on the surface of CP@SIM coated Zn alloy and the surface morphology of these bacteria was changed and damaged, which showed a wrinkled and
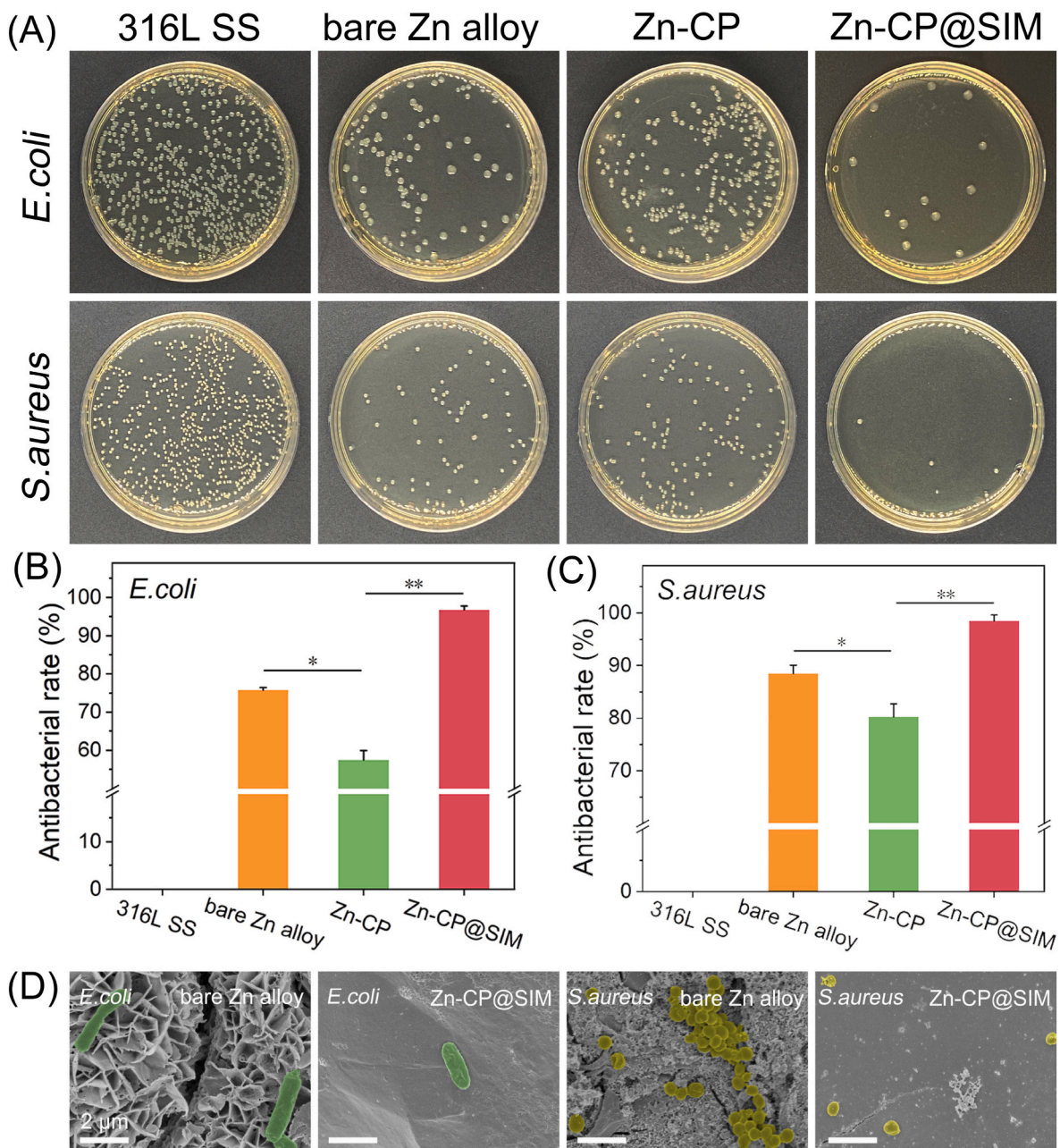
Fig. 6. Antibacterial activity of 316L SS and different Zn alloys samples against *E. coli* and *S. aureus*. (A) Photographs of agar plates of colonies of *E. coli* and *S. aureus*. The antibacterial rate of different samples against (B) *E. coli* and (C) *S. aureus*. (D) The SEM images of the morphological changes of *E. coli* and *S. aureus* after incubation with bare Zn alloy and Zn-CP@SIM samples. *$p < 0.05$, **$p < 0.01$.

distorted surface. This further indicated that the CP@SIM coated Zn alloy inhibited the bacterial growth and biofilm formation with the combined antibacterial effect of Zn^{2+} and SIM.

3.7. In vivo experiments

To further study the biocompatibility, and *in vivo* promoting new bone formation and vascularization functions of the coatings, bare and coated cylindrical Zn alloys samples were implanted into a rabbit femoral defect with critical size. The 2D and 3D micro-CT images of the implants and surrounding bones at 8 weeks after implantation were analyzed (Fig. 7A). New bone tissue (white) was found on the surface of all implants (yellow), demonstrating the development of bone regeneration. Surprisingly, the bare Zn alloys also showed a bone repair capability, which to some extent highlighted the advantages of biodegradable Zn–Li alloys for utilization as bone implants. As expect, the Zn-CP@SIM exhibited the best osteogenesis promoting performance that the Zn-CP@SIM implant was nearly fully covered by the new bone tissue. Quantitative analysis of new bone volume (BV/TV) and new bone mineral density (BS/TV) calculated from the micro-CT were assessed (Fig. 7B and C). Compared to bare Zn alloys, coated Zn alloys had more newborn bone tissue and higher bone mineral density, which was consistent with the findings from the *in vitro* osteogenic test. Notably, the CP@SIM coated Zn alloys exhibited the best bone repair capability compared to the other two samples, which could be explained by the following two main reasons. On the one hand, the CP@SIM coating ensured that the Zn^{2+} concentration at the implant site was not too high to hinder bone regeneration by inhibiting Zn^{2+} release, which improved the biocompatibility of the Zn alloy surfaces, providing a microenvironment conductive to adherence and growth of osteoclasts. On the other hand, the CP@SIM coating showed a sustained release of osteogenic favorably SIM. These two functions synergistically facilitated the bone repair process.

Histological H&E staining and Masson's trichrome staining were conducted to further confirm the coating's performance on *in vivo* new bone formation (Fig. 8). The H&E staining images showed the newly formed tissue in the entire femoral defect after 8 weeks surgery. Compared with many predominantly fibrous tissues observed in bare Zn alloy group, Zn-CP@SIM group showed less fibrous tissue and more dense new bone. As seen in the enlarged images, Zn-CP@SIM group had significantly more round holes in the new bone tissue than the other two groups, implying that more vascular tissue (black arrows) was formed. These results further demonstrated that the combination of low dose of Zn^{2+} and uniformly release of SIM synergistically promoted new bone formation and vascularization. Meanwhile, no obverse inflammatory reaction was found in both coated Zn alloy groups, which indicated the good *in vivo* biocompatibility and antibacterial effect of coatings. In Masson's trichrome staining, collagen fibers and cartilage appear blue, while muscle fibers and erythrocytes are red [64]. Like the observation from the H&E staining, the results of Masson's trichrome staining revealed that a large amount of mineralized collagen fibers (blue color) and conspicuous neovascularization (black arrows) were generated in Zn-CP@SIM group, reflecting much more collagen deposition and new blood vessel formation, which further confirmed the excellent osseointegration of the drug-eluting coating on Zn alloys. The immunohistochemical staining of ossification-related osteocalcin (OCN) and vascularization-related platelet endothelial cell adhesion molecule-1 (CD31) was conducted to further confirm the coating's performance on *in vivo* new bone formation and vascularization (Fig. 8). OCN is a highly specific marker for osteoblasts and is commonly used to assess the extent of bone formation [65]. CD31 is generally regarded as a marker of endothelial cell lineage, and upregulation of its expression implies an enhanced angiogenic effect [66]. The expression of OCN and CD31 was measured by immunohistochemical staining after 8 weeks of implantation. The OCN- and CD31-positive staining of Zn-CP@SIM group was more pronounced than Zn-CP and bare Zn alloy groups, reflecting high
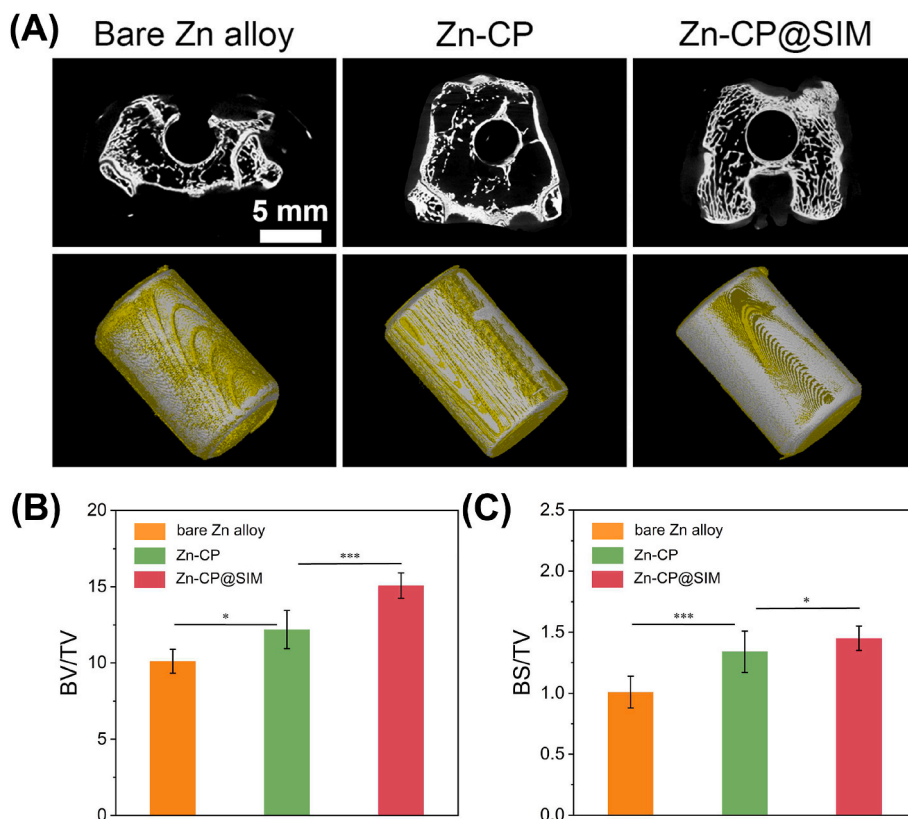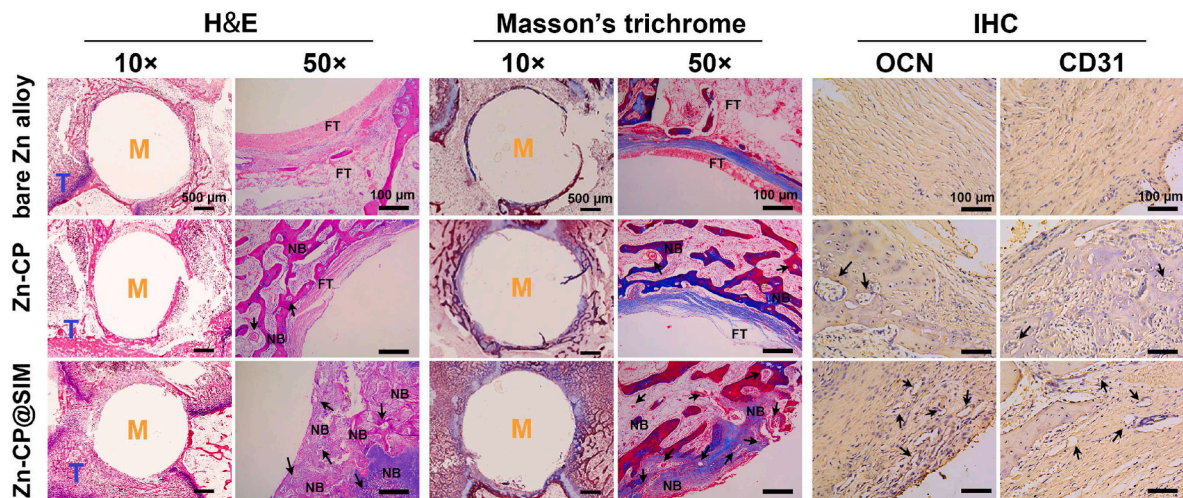

Fig. 7. Results of the rabbit critical-size femur defect model. (A) 2D and 3D micro-CT images of the implants and surrounding bones. Quantification of (B) new bone volume and (C) new bone mineral density. $*p < 0.05$, $**p < 0.01$, $***p < 0.001$.

Fig. 8. Representative photographs of histological staining of H&E and Masson's trichrome, and immunohistochemical staining of OCN and CD31 after implanting 8 weeks. M = metal; T = tissue; FT = fibrous tissue; NB = newly formed bone; Black arrows = blood vessels.

level of bone formation and vascularization, which was consistent with the results of H&E and Masson's trichrome staining. Above findings demonstrated that CP@SIM coated Zn alloys could efficiently enhance the biocompatibility, osteogenesis, and angiogenesis of Zn alloys *in vivo*.

4. Conclusions

In this work, an imidazole functionalized biodegradable aliphatic polycarbonate drug-eluting coating Zn-CP@SIM was fabricated by EPD method on Zn–Li alloys to inhibit Zn^{2+} release and enhance the osteogenesis, angiogenesis, and bacteriostasis of Zn alloys. Compared with the commercially available PTMC coating, Zn-CP@SIM coatings had better mechanical properties. In long-term immersion experiments, compared with commercially available PLGA coating, Zn-CP@SIM coatings shows a regulated Zn^{2+} release property and more stable SIM release curves, maintaining coating integrity even after 60 days of immersion. Zn-CP@SIM coatings could effectively reduce the cytotoxicity of zinc alloy substrate, and provide a good biological microenvironment for the adhesion, spread and differentiation of osteoblasts. In addition, Zn-CP@SIM coatings showed excellent angiogenic and antibacterial properties, with an antibacterial rates of over 95% against both *E.coli* and *S.aureus*. Finally, *in vivo* animal studies showed that Zn-CP@SIM coatings had a less inflammatory response and more collagen deposition, effectively promoting the expression of platelet-endothelial cell adhesion molecules (CD31) and osteocalcin (OCN).

Ethics approval and consent to participate

All procedures of the experiment were approved and in accordance with the committee of the Wuxi Experimental Animal Association.

CRediT authorship contribution statement

Wei Zhang: Writing – original draft, Software. **Miao Dai:** Investigation. **Ye Zhu:** Writing – review & editing, Methodology. **Siyuan Li:** Validation. **Ying Sun:** Validation. **Xiaoya Liu:** Methodology, Funding acquisition. **Xiaojie Li:** Writing – review & editing, Methodology, Funding acquisition.

Declaration of competing interest

The authors declare no conflicts of interest.

Appendix A. Supplementary data

Supplementary data to this article can be found online at https://doi.org/10.1016/j.bioactmat.2024.03.037.

References

[1] G.L. Koons, M. Diba, A.G. Mikos, Materials design for bone-tissue engineering, Nat. Rev. Mater. 5 (8) (2020) 584–603.

[2] M.M. Stevens, Biomaterials for bone tissue engineering, Mater. Today 11 (5) (2008) 18–25.

[3] J. Zhang, Y. Jiang, Z. Shang, B. Zhao, M. Jiao, W. Liu, M. Cheng, B. Zhai, Y. Guo, B. Liu, X. Shi, B. Ma, Biodegradable metals for bone defect repair: a systematic review and meta-analysis based on animal studies, Bioact. Mater. 6 (11) (2021) 4027–4052.

[4] X. Zhang, Y. Li, Y.E. Chen, J. Chen, P.X. Ma, Cell-free 3D scaffold with two-stage delivery of miRNA-26a to regenerate critical-sized bone defects, Nat. Commun. 7 (1) (2016) 10376.

[5] R.T. Annamalai, X. Hong, N.G. Schott, G. Tiruchinapally, B. Levi, J.P. Stegemann, Injectable osteogenic microtissues containing mesenchymal stromal cells conformally fill and repair critical-size defects, Biomaterials 208 (2019) 32–44.

[6] E.H. Schemitsch, Size Matters: defining critical in bone defect size, J. Orthop. Trauma 31 (2017) S20–S22.

[7] J. Zhang, W. Liu, V. Schnitzler, F. Tancret, J.-M. Bouler, Calcium phosphate cements for bone substitution: chemistry, handling and mechanical properties, Acta Biomater. 10 (3) (2014) 1035–1049.

[8] E. García-Gareta, M.J. Coathup, G.W. Blunn, Osteoinduction of bone grafting materials for bone repair and regeneration, Bone 81 (2015) 112–121.

[9] P.V. Giannoudis, H. Dinopoulos, E. Tsiridis, Bone substitutes: an update, Injury 36 (3, Supplement) (2005) S20–S27.

[10] C. Xiao, X.Y. Shi, W.T. Yu, X.W. Wei, L.L. Cheng, X. Qiu, B.R. Li, D.C. Fan, J.L. Li, X. Z. Zhang, D.W. Zhao, In vivo biocompatibility evaluation of Zn-0.05Mg-(0, 0.5, 1wt%)Ag implants in New Zealand rabbits, Mater. Sci. Eng. C 119 (2021) 111435.

[11] X. Tong, Y. Han, R.Q. Zhou, J. Zeng, C. Wang, Y.F. Yuan, L. Zhu, S.B. Huang, J. F. Ma, Y.C. Li, C.E. Wen, J.X. Lin, Mechanical properties, corrosion and degradation behaviors, and in vitro cytocompatibility of a biodegradable Zn-5La alloy for bone-implant applications, Acta Biomater. 169 (2023) 641–660.

[12] Y.F. Zheng, X.N. Gu, F. Witte, Biodegradable metals, Mater. Sci. Eng. R 77 (2014) 1–34.

[13] H.-S. Han, S. Loffredo, I. Jun, J. Edwards, Y.-C. Kim, H.-K. Seok, F. Witte, D. Mantovani, S. Glyn-Jones, Current status and outlook on the clinical translation of biodegradable metals, Mater. Today 23 (2019) 57–71.

[14] P.K. Bowen, E.R. Shearier, S. Zhao, R.J. Guillory Ii, F. Zhao, J. Goldman, J. W. Drelich, Biodegradable metals for cardiovascular stents: from clinical concerns to recent Zn-alloys, Adv. Healthcare Mater. 5 (10) (2016) 1121–1140.

[15] K. Chen, X.N. Gu, Y.F. Zheng, Feasibility, challenges and future prospects of biodegradable zinc alloys as orthopedic internal fixation implants, Smart Mater. Manuf. 2 (2024) 100042.

[16] H.T. Yang, B. Jia, Z.C. Zhang, X.H. Qu, G.N. Li, W.J. Lin, D.H. Zhu, K.R. Dai, Y. F. Zheng, Alloying design of biodegradable zinc as promising bone implants for load-bearing applications, Nat. Commun. 11 (1) (2020) 401.

[17] W. Yuan, D.D. Xia, Y.F. Zheng, X.M. Liu, S.L. Wu, B. Li, Y. Han, Z.J. Jia, D.H. Zhu, L.Q. Ruan, K. Takashima, Y.S. Liu, Y.S. Zhou, Controllable biodegradation and enhanced osseointegration of ZrO2-nanofilm coated Zn-Li alloy: in vitro and in vivo studies, Acta Biomater. 105 (2020) 290–303.

[18] H.T. Yang, X.H. Qu, M.Q. Wang, H.W. Cheng, B. Jia, J.F. Nie, K.R. Dai, Y.F. Zheng, Zn-0.4Li alloy shows great potential for the fixation and healing of bone fractures at load-bearing sites, Chem. Eng. J. 417 (2021) 129317.

[19] D. Zhu, Y. Su, M.L. Young, J. Ma, Y. Zheng, L. Tang, Biological responses and mechanisms of human bone marrow mesenchymal stem cells to Zn and Mg biomaterials, ACS Appl. Mater. Interfaces 9 (33) (2017) 27453–27461.

[20] H. Yang, X. Qu, W. Lin, D. Chen, D. Zhu, K. Dai, Y. Zheng, Enhanced osseointegration of Zn-Mg composites by tuning the release of Zn ions with sacrificial Mg-rich anode design, ACS Biomater. Sci. Eng. 5 (2) (2019) 453–467.

[21] J. He, J. Fang, P. Wei, Y. Li, H. Guo, Q. Mei, F. Ren, Cancellous bone-like porous Fe@Zn scaffolds with core-shell-structured skeletons for biodegradable bone implants, Acta Biomater. 121 (2021) 665–681.

[22] Z. Chen, W. Zhang, M. Wang, L.J. Backman, J. Chen, Effects of zinc, magnesium, and iron ions on bone tissue engineering, ACS Biomater. Sci. Eng. 8 (6) (2022) 2321–2335.

[23] N. Yang, J. Venezuela, S. Almathami, M. Dargusch, Zinc-nutrient element based alloys for absorbable wound closure devices fabrication: current status, challenges, and future prospects, Biomaterials 280 (2022) 121301.

[24] C. Wang, J.H. Lai, K. Li, S.K. Zhu, B.H. Lu, J. Liu, Y.J. Tang, Y. Wei, Cryogenic 3D printing of dual-scale scaffolds for improved bone regeneration with enhanced vascularization, Bioact. Mater. 6 (1) (2021) 137–145.

[25] J.Y. Qian, W.T. Zhang, Y.Q. Chen, P.J. Zeng, J.L. Wang, C. Zhou, H. Zeng, H. X. Sang, N. Huang, H.J. Zhang, G.J. Wan, Osteogenic and angiogenic bioactive collagen entrapped calcium/zinc phosphates coating on biodegradable Zn for orthopedic implant applications, Biomater, Adv 136 (2022) 212792.

[26] C.D. Gao, M. Yao, S.P. Peng, W. Tan, C.J. Shuai, Pre-oxidation induced in situ interface strengthening in biodegradable Zn/nano-SiC composites prepared by selective laser melting, J. Adv. Res. 38 (2022) 143–155.

[27] T. Huang, Z.L. Liu, D.C. Wu, H.L. Yu, Microstructure, mechanical properties, and biodegradation response of the grain-refined Zn alloys for potential medical materials, J. Mater. Res. Technol. 15 (2021) 226–240.

[28] L.S. Zhang, X. Tong, J.X. Lin, Y.C. Li, C. Wen, Enhanced corrosion resistance via phosphate conversion coating on pure Zn for medical applications, Corrosion Sci. 169 (2020) 108602.

[29] Y.Y. Sheng, J.J. Yang, X.Y. Zhao, H. Liu, S.G. Cui, L.X. Chen, R. Zeng, X.J. Wang, C. H. Huang, W. Li, Development and in vitro biodegradation of biomimetic zwitterionic phosphorylcholine chitosan coating on Zn1Mg alloy, ACS Appl. Mater. Interfaces 12 (49) (2020) 54445–54458.

[30] K. Pan, W. Zhang, H. Shi, M. Dai, Z. Yang, M. Chen, W. Wei, Y. Zheng, X. Liu, X. Li, Facile fabrication of biodegradable endothelium-mimicking coatings on bioabsorbable zinc-alloy stents by one-step electrophoretic deposition, J. Mater. Chem. B 10 (16) (2022) 3083–3096.

[31] K. Pan, W. Zhang, H. Shi, M. Dai, W. Wei, X. Liu, X. Li, Zinc Ion-crosslinked polycarbonate/heparin composite coatings for biodegradable Zn-alloy stent applications, Colloid Surf. B-Biointerfaces 218 (2022) 112725.

[32] E. Jablonská, D. Vojtěch, M. Fousová, J. Kubásek, J. Lipov, J. Fojt, T. Ruml, Influence of surface pre-treatment on the cytocompatibility of a novel biodegradable ZnMg alloy, Mater. Sci. Eng. C 68 (2016) 198–204.

[33] Y. Zhuang, Q.C. Liu, G.Z. Jia, H.L. Li, G.Y. Yuan, H.B. Yu, A biomimetic zinc alloy scaffold coated with brushite for enhanced cranial bone regeneration, ACS Biomater. Sci. Eng. 7 (3) (2021) 893–903.

[34] G.K. Katarivas Levy, A. Kafri, Y. Ventura, A. Leon, R. Vago, J. Goldman, E. Aghion, Surface stabilization treatment enhances initial cell viability and adhesion for biodegradable zinc alloys, Mater. Lett. 248 (2019) 130–133.

[35] W. Yuan, B. Li, D.F. Chen, D.H. Zhu, Y. Han, Y.F. Zheng, Formation mechanism, corrosion behavior, and cytocompatibility of microarc oxidation coating on absorbable high-purity zinc, ACS Biomater. Sci. Eng. 5 (2) (2018) 487–497.

[36] F. Peng, Y.L. Lin, D.D. Zhang, Q.D. Ruan, K.W. Tang, M. Li, X.Y. Liu, P.K. Chu, Y. Zhang, Corrosion behavior and biocompatibility of diamond-like carbon-coated zinc: an in vitro study, ACS Omega 6 (14) (2021) 9843–9851.

[37] P. Li, J.Y. Qian, W.T. Zhang, C. Schille, E. Schweizer, A. Heiss, U.E. Klotz, L. Scheideler, G.J. Wan, J. Geis-Gerstorfer, Improved biodegradability of zinc and its alloys by sandblasting treatment, Surf. Coating. Technol. 405 (2021) 126678.

[38] L. Tan, X. Wang, K. Yuan, T. Yin, R. Du, L. Shen, Z. Zhu, S. Yu, H. Zhang, G. Wang, Structural and temporal dynamics analysis on drug-eluting stents: history, research hotspots and emerging trends, Bioact. Mater. 23 (2023) 170–186.

[39] H. Jin, Y.B. Ji, Y.T. Cui, L. Xu, H. Liu, J.C. Wang, Simvastatin-incorporated drug delivery systems for bone regeneration, ACS Biomater. Sci. Eng. 7 (6) (2021) 2177–2191.

[40] T.T. Sun, J. Huang, W. Zhang, X.Q. Zheng, H. Wang, J. Liu, H.J. Leng, W.Q. Yuan, C.L. Song, Simvastatin-hydroxyapatite coatings prevent biofilm formation and improve bone formation in implant-associated infections, Bioact. Mater. 21 (2023) 44–56.

[41] X. Wang, O. Ronsin, B. Gravez, N. Farman, T. Baumberger, F. Jaisser, T. Coradin, C. Hélary, Nanostructured dense collagen-polyester composite hydrogels as amphiphilic platforms for drug delivery, Adv. Sci. 8 (7) (2021) 2004213.

[42] Y. Xu, C.-S. Kim, D.M. Saylor, D. Koo, Polymer degradation and drug delivery in PLGA-based drug-polymer applications: a review of experiments and theories, J. Biomed. Mater. Res. B 105 (6) (2017) 1692–1716.

[43] W. Yu, E. Maynard, V. Chiaradia, M.C. Arno, A.P. Dove, Aliphatic polycarbonates from cyclic carbonate monomers and their application as biomaterials, Chem. Rev. 121 (18) (2021) 10865–10907.

[44] I. Ansari, P. Singh, A. Mittal, R.I. Mahato, D. Chitkara, 2,2-Bis(hydroxymethyl) propionic acid based cyclic carbonate monomers and their (co)polymers as advanced materials for biomedical applications, Biomaterials 275 (2021) 120953.

[45] D. Mozhdehi, J.A. Neal, S.C. Grindy, Y. Cordeau, S. Ayala, N. Holten-Andersen, Z. Guan, Tuning dynamic mechanical response in metallopolymer networks through simultaneous control of structural and temporal properties of the networks, Macromolecules 49 (17) (2016) 6310–6321.

[46] J.A. Neal, N.J. Oldenhuis, A.L. Novitsky, E.M. Samson, W.J. Thrift, R. Ragan, Z. Guan, Large continuous mechanical gradient formation via metal–ligand interactions, Angew. Chem. Int. Ed. 56 (49) (2017) 15575–15579.

[47] W. Maret, Y. Li, Coordination dynamics of zinc in proteins, Chem. Rev. 109 (10) (2009) 4682–4707.

[48] K. Naka, S. Masuoka, R. Shinke, M. Yamada, Synthesis of first- and second-generation imidazole-terminated POSS-core dendrimers and their pH responsive and coordination properties, Polym. J. 44 (4) (2012) 353–359.

[49] D. Mozhdehi, S. Ayala, O.R. Cromwell, Z.B. Guan, Self-healing multiphase polymers via dynamic metal–ligand interactions, J. Am. Chem. Soc. 136 (2014) 16128–16131.

[50] T. Xie, J. Ding, X.X. Han, H.Z. Jia, Y. Yang, S. Liang, W.X. Wang, W.G. Liu, W. Wang, Wound dressing change facilitated by spraying zinc ions, Mater. Horiz. 7 (2020) 605–614.

[51] K. Pan, X. Li, H. Shi, M. Dai, Z. Yang, M. Chen, W. Wei, X. Liu, Y. Zheng, Preparation of photo-crosslinked aliphatic polycarbonate coatings with predictable degradation behavior on magnesium-alloy stents by electrophoretic deposition, Chem. Eng. J. 427 (2022) 131596.

[52] D.P. Sanders, K. Fukushima, D.J. Coady, A. Nelson, M. Fujiwara, M. Yasumoto, J. L. Hedrick, A simple and efficient synthesis of functionalized cyclic carbonate monomers using a versatile pentafluorophenyl ester intermediate, J. Am. Chem. Soc. 132 (42) (2010) 14724–14726.

[53] D. Trel'ová, A.R. Salgarella, L. Ricotti, G. Giudetti, A. Cutrone, P. Šrámková, A. Zahoranová, D. Chorvát Jr., D. Haško, C. Canale, S. Micera, J. Kronek, A. Menciassi, I. Lacík, Soft hydrogel zwitterionic coatings minimize fibroblast and macrophage adhesion on polyimide substrates, Langmuir 35 (5) (2019) 1085–1099.

[54] X.-C. Chen, W.-P. Huang, K.-F. Ren, J. Ji, Self-healing label materials based on photo-cross-linkable polymeric films with dynamic surface structures, ACS Nano 12 (8) (2018) 8686–8696.

[55] B.J.C. Thomas, A.R. Boccaccini, M.S.P. Shaffer, Multi-walled carbon nanotube coatings using electrophoretic deposition (EPD), J. Am. Ceram. Soc. 88 (4) (2005) 980–982.

[56] D.N. Kapoor, A. Bhatia, R. Kaur, R. Sharma, G. Kaur, S. Dhawan, PLGA: a unique polymer for drug delivery, Ther. Deliv. 6 (1) (2015) 41–58.

[57] H.T. Yang, C. Wang, C.Q. Liu, H.W. Chen, Y.F. Wu, J.T. Han, Z.C. Jia, W.J. Lin, D. Y. Zhang, W.T. Li, W. Yuan, H. Guo, H.F. Li, G.X. Yang, D.L. Kong, D.H. Zhu, K. Takashima, L.Q. Ruan, J.F. Nie, X. Li, Y.F. Zheng, Evolution of the degradation mechanism of pure zinc stent in the one-year study of rabbit abdominal aorta model, Biomaterials 145 (2017) 92–105.

[58] H. Kabir, K. Munir, C. Wen, Y. Li, Recent research and progress of biodegradable zinc alloys and composites for biomedical applications: biomechanical and biocorrosion perspectives, Bioact. Mater. 6 (3) (2021) 836–879.

[59] H. Tang, H. Li, Y. Zhao, C. Liu, X. Gu, Y. Fan, A surface-eroding poly(1,3-trimethylene carbonate) coating for magnesium based cardiovascular stents with stable drug release and improved corrosion resistance, Bioact. Mater. 7 (2022) 144–153.

[60] T. Xiao, L. Fan, R. Liu, X. Huang, S. Wang, L. Xiao, Y. Pang, D. Li, J. Liu, Y. Min, Fabrication of dexamethasone-loaded dual-metal-organic frameworks on polyetheretherketone implants with bacteriostasis and angiogenesis properties for promoting bone regeneration, ACS Appl. Mater. Interfaces 13 (43) (2021) 50836–50850.

[61] J. Qin, D. Yang, S. Maher, L. Lima-Marques, Y. Zhou, Y. Chen, G.J. Atkins, D. Losic, Micro- and nano-structured 3D printed titanium implants with a hydroxyapatite coating for improved osseointegration, J. Mater. Chem. B 6 (19) (2018) 3136–3144.

[62] S.S. Zhao, W.Y. Dong, Y.L. Wang, X.Y. Zhou, J.H. Jiang, R.B. Hu, T. Lin, D.H. Sun, M. Zhang, Construction of multifunctional zinc ion sustained-release biocoating on the surface of carbon fiber reinforced polyetheretherketone with enhanced anti-inflammatory activity, angiogenesis, and osteogenesis, ACS Appl. Mater. Interfaces 15 (26) (2023) 31256–31272.

[63] H.T. Yang, X.H. Qu, W.J. Lin, C. Wang, D.J. Zhu, K.R. Dai, Y.F. Zheng, In vitro and in vivo studies on zinc-hydroxyapatite composites as novel biodegradable metal matrix composite for orthopedic applications, Acta Biomater. 71 (2018) 200–214.

[64] M. Wu, F. Chen, P. Wu, Z. Yang, S. Zhang, L. Xiao, Z. Deng, C. Zhang, Y. Chen, L. Cai, Bioinspired redwood-like Scaffolds coordinated by in situ-generated silica-containing hybrid nanocoatings promote angiogenesis and osteogenesis both in vitro and in vivo, Adv. Healthcare Mater. 10 (23) (2021) 2101591.

[65] C. Gundberg, Biology, physiology, and clinical chemistry of osteocalcin, J. Clin. Ligand Assay 21 (2) (1998) 128–138.

[66] S. Kim, H. Kim, Y. Yoon, Advances in bone marrow-derived cell therapy: CD31-expressing cells as next generation cardiovascular cell therapy, Regen. Med. 6 (3) (2011) 335–349.